Simulations of cloud-radiation interaction using large-scale forcing derived from the CINDY/DYNAMO northern sounding array

Shuguang Wang[1], Adam H. Sobel[1,2,3], Ann Fridlind[4], Zhe Feng[5], Jennifer M. Comstock[5], Patrick Minnis[6], Michele L. Nordeen[7]

1 Department of Applied Physics and Applied Mathematics, Columbia University, New York, NY

2 Lamont-Doherty Earth Observatory of Columbia University, Palisades, NY

3 Department of Earth and Environmental Sciences, Columbia University, New York, NY

4 NASA Goddard Institute for Space Studies, New York, NY

5 Pacific Northwest National Laboratory, Richland, Washington

6 NASA Langley Research Center, Hampton, VA

7 Science Systems and Applications, Inc., Hampton, VA

Submitted to *Journal of Advances in Modeling Earth Systems*

March 2015

Abstract

The recently completed CINDY/DYNAMO field campaign observed two Madden-Julian oscillation (MJO) events in the equatorial Indian Ocean from October to December 2011. Prior work has indicated that the moist static energy anomalies in these events grew and were sustained to a significant extent by radiative feedbacks. We present here a study of radiative fluxes and clouds in a set of cloud-resolving simulations of these MJO events. The simulations are driven by the large scale forcing dataset derived from the DYNAMO northern sounding array observations, and carried out in a doubly-periodic domain using the Weather Research and Forecasting (WRF) model. Simulated cloud properties and radiative fluxes are compared to those derived from the S-Polka radar and satellite observations. To accommodate the uncertainty in simulated cloud microphysics, a number of single moment (1M) and double moment (2M) microphysical schemes in the WRF model are tested.

The 1M schemes tend to underestimate radiative flux anomalies in the active phases of the MJO events, while the 2M schemes perform better, but can overestimate radiative flux anomalies. All the tested microphysics schemes exhibit biases in the shapes of the histograms of radiative fluxes and radar reflectivity. Histograms of radiative fluxes and brightness temperature indicate that radiative biases are not evenly distributed; the most significant bias occurs in rainy areas with OLR less than 150 W/m^2 in the 2M schemes. Analysis of simulated radar reflectivities indicates that this radiative flux uncertainty is closely related to the simulated stratiform cloud coverage. Single moment schemes underestimate stratiform cloudiness by a factor of two, whereas 2M schemes simulate much more stratiform cloud.

1. Introduction

The Madden Julian Oscillation (MJO) is the dominant intra-seasonal variability in the tropical atmosphere [*Madden and Julian* 1971, 1972]. It is a large-scale (zonal wavenumber of 1 or 2), eastward-propagating (at ~5 m s^{-1}) system that influences rainfall over virtually all of the tropics and subtropics. The MJO impacts many aspects of weather and climate over the globe, including El Niño-Southern Oscillation (ENSO) variability [*Pohl and Matthews* 2007; *Zhang and Gottschalck* 2002; *Zhang* 2005], tropical cyclogenesis [*Maloney and Hartmann* 2000; *Hall et al.* 2001; *Bessafi et al.* 2006; *Vitart* 2009; *Camargo et al.* 2009; *Huang et al.* 2011], global angular momentum [*Langley et al.* 1981; *Weickmann and Berry* 2009], Asian and North American monsoon systems [*Zhang and Dong* 2004; *Wheeler and McBride* 2005], North American extreme precipitation events (e.g., *Jones* [2000]), the North Atlantic Oscillation and mid-latitude storm tracks [*Cassou* 2008; *Lin et al.* 2009], Arctic temperature anomalies [*Yoo et al.* 2011], and sudden stratospheric warming events [*Garfinkel et al.* 2012] in the polar regions. These studies thus suggest that understanding the physical processes in the MJO is critical for better modeling of climate variability and large-scale weather events.

Despite decades of research, there is no consensus on the fluid dynamics of the MJO. A number of studies assert that the MJO is a "moisture mode" (e.g., *Sobel et al.* [2001], *Fuchs and Raymond* [2002], *Sugiyama* [2009], *Bony and Emanuel* [2005], *Sobel and Maloney* [2012, 2013]), meaning, a mode with no analog in a dry atmosphere which emerges due to the presence of moisture and feedbacks associated with diabatic processes. The processes that maintain the MJO, to the extent that it is a moisture mode, are those that reinforce moist static energy (MSE) MJO anomalies. This occurs when a positive MSE anomaly, for example, induces either diabatic or advective processes, which lead to a positive local MSE tendency. The most important

47 diabatic feedback processes, those that act as sources or sinks for MSE, are surface fluxes (e.g.,
48 Emanuel [1987]; *Neelin et al.* [1987]) and radiative transfer. Much modeling and theoretical
49 work indicates that radiative-convective feedbacks are important to the MJO (e.g., *Raymond*
50 [2001]; *Grabowski* [2003]; *Bony and Emanuel* [2005]; *Sobel et al.* [2008, 2010, 2014]; *Andersen*
51 *and Kuang* [2012]; *Kim et al*. [2011], *Chikira* [2014]). In this study, we focus on cloud formation,
52 and radiative transfer, and their interaction during two MJO events.

53 During its active phase, the most prominent feature of the MJO viewed from space is its
54 extensive spreading cloud systems that cover broad regions of the deep tropics. These clouds
55 dominate the transfer of solar and infrared radiation, reducing the radiative cooling of the
56 atmospheric column [*Johnson and Ciesielski* 2000; *Ma and Kuang* 2011; *Sobel et al.* 2014]. The
57 observational analysis by *Lin and Mapes* (2004) quantified the relationship between diabatic
58 heating and radiation anomalies in the MJO, finding that a given convective heating anomaly is
59 associated with a radiative heating anomaly having the same sign and 10-15% of its magnitude.
60 In simple models described by *Sobel and Gildor* [2003], and *Sobel and Maloney* [2012, 2013]
61 this feedback is essential to the instability mechanisms of the intraseasonal oscillations, and
62 *Sobel et al.* [2008, 2010] argued that this is consistent with observations and more
63 comprehensive model simulations.

64 Consistent with this, a number of experiments with general circulation models [*Lee et al.*
65 2001; *Kim et al.* 2011; *Anderson and Kuang* 2012; *Chikira* 2014] also suggest that radiative
66 feedback is important in simulating the MJO. Some studies have further pointed to the
67 importance of specific cloud types. In particular, greater stratiform cloud coverage (for a given
68 level of convective activity) leads to better MJO simulation (e.g., *Fu and Wang* [2009]; *Seo and*
69 *Wang* [2010]; *Lee et al.* [2001]; *Kim et al.* [2011]). However, large uncertainties in the simulated

70 cloud microphysics, itself related in part to the lack of adequate observational constraints, make
71 it difficult to evaluate these simulations.
72 The present study focuses on the cloud and radiation fields observed during two MJO
73 events in the central Indian Ocean in the recent field campaigns for the Cooperative Indian
74 Ocean Experiment on Intraseasonal Variability (CINDY)/Dynamics of the MJO
75 (DYNAMO)/ARM MJO Investigation Experiment (AMIE), hereafter "DYNAMO" for brevity
76 [*Zhang et al.* 2013, *Yoneyama et al.* 2014; *Gottschal*ck et al. 2013]. Analysis of the in-situ radar
77 data shows abundant, expansive stratiform clouds [*Powell and Houze* 2013, *DePasquale et al.*
78 2014] during the active phases of the DYNAMO MJO events. The moist static energy (MSE)
79 budget analysis of *Sobel et al.* [2014] indicates that the contribution of the radiation anomaly to
80 the column integrated MSE budget is stronger than that of the surface enthalpy flux. We expect
81 that the expansive stratiform clouds contributed greatly to radiation anomaly. On the other hand,
82 the skill of numerical models to faithfully reproduce those clouds has not been well tested using
83 these field observations. Here we perform numerical simulations and compare the simulated
84 cloud and radiation fields to observations.
85 We will present a set of cloud-resolving model (CRM) simulations driven by the
86 DYNAMO northern sounding array (NSA) forcing with different cloud microphysics schemes.
87 We attempt to address the following questions: Can we faithfully simulate radiative fluxes and
88 net column radiation using the state-of-the-art high resolution numerical model? What aspects of
89 cloud microphysics are responsible for bias and uncertainty in simulated radiative fluxes? Can
90 the WRF-CRM capture the observed radar echo structure and convective/stratiform separation?
91 What microphysical treatment has the best skill in simulating cloud-radiation feedback? This rest

of the paper is structured as follows. Simulations and observations will be described in Section 2, followed by results in Section 3.

2. Numerical experimental design and observational dataset

2.1 The DYNAMO northern sounding array forcing

The DYNAMO NSA was located mostly north of the equator in the central equatorial Indian Ocean, and experienced coherent variability in deep convection associated with two active MJO phases during late October and early November, 2011. Four sounding sites constituting the NSA were deployed from 1 October to 15 December, 2011, located at Gan Island, Maldives (0.698°N, 73.518°E), Malé, Maldives (4.918°N, 73.538°E), Colombo, Sri Lanka (6.918°N, 79.878°E), and on the R/V Revelle (0.008°, 80.508°E). Because the R/V Revelle was off station from 31 October to 7 November, and 8-15 December, the ECMWF-Interim reanalysis data were additionally used to derive the forcing dataset during those two periods [*Johnson and Ciesielski* 2013; *Johnson et al.* 2015].

Large-scale ascent and horizontal advection of moisture and temperature derived from the NSA [*Johnson and Ciesielski,* 2013] are used to drive the numerical simulations discussed below. Figure 1a displays strong large-scale ascent peaking at 10 – 12 km during the active phases, and weak large-scale descent in the suppressed phases. Drying is pronounced at the beginning of October and reaches 3-4 g/kg/day toward the end of November. Daily sea surface temperature is relatively low (28.7 $^{\circ}$C) in early October and varies less than 0.5 $^{\circ}$C for the most of period, but warms up by 0.5 $^{\circ}$C during the suppressed phases in the first two weeks of November.

2.2 Numerical experiment design

114 The WRF model V3.5.1 [*Skamarock et al.,* 2008] is adopted to perform cloud-resolving
115 simulations with doubly-periodic lateral boundary conditions. The simulations are driven by the
116 large-scale forcing dataset (version 1) derived from the DYNAMO northern sounding array
117 observations [*Johnson and Ciesielski* 2013, *Ciesielski et al.* 2014]. As in a number of past works
118 (e.g., *Grabowski et al.* [1996]; *Wu et al.* [1998]; *Xu and Randall* [2001]; *Tao et al.* [2004];
119 *Khairoutdinov and Randall* [2003]; *Blossey et al.* [2007]; *Varble et al.* [2011]; *Fridlind et al.*
120 [2012], *Mrowiec et al.* [2012], *Janiga and Zhang* [2015]), large scale vertical velocity is used to
121 advect horizontally averaged variables (potential temperature and moisture) in the dry mass
122 vertical coordinate, and observationally derived horizontal advective tendencies of these
123 variables by the large-scale flow are imposed. No forcing is used for any liquid and ice
124 hydrometeors. The lower boundary condition is the daily sea surface temperature. The domain-
125 averaged wind profiles are relaxed to the observed values averaged over NSA using a relaxation
126 time scale of 1 hour. This provides constraints on surface fluxes and, to a lesser degree, on
127 convective organization.
128 As the dominant large-scale dynamics are specified in this modeling approach, feedback
129 processes, such as surface fluxes or radiation, have little effect on surface rain rates. Thus, this
130 approach allows us to isolate biases in these processes from biases in the large scale dynamics.
131 The present study will focus on cloud-radiative interaction. Our semi-idealized column modeling
132 setup of WRF as a CRM differs from its typical usage in regional simulations with prescribed
133 tendencies at the lateral boundaries and multiple-level nesting to achieve high resolution, but this
134 regular setup often struggles to simulate surface rain rates at the correct timings and locations.
135 The TWP-ICE model inter-comparison project offers an excellent exposition of this issue [*Zhu et*
136 *al*. 2012; *Petch et al.* 2014].

137 The microphysical transformation predicts the amount of each hydrometeor species.
138 Among the many options available in WRF, we choose a subset of the bulk microphysics
139 schemes, including two single-moment (1M) schemes: PLin [*Lin et al.* 1983; *Chen and Sun* 2002]
140 and WSM6 [*Hong and Lim* 2006] and four double-moment microphysics (2M) schemes:
141 Thompson [*Thompson et al.* 2008], Morrison [*Morrison et al.* 2009, hereafter M09], MY05
142 [*Milbrandt and Yau* 2005], and WDM6 [*Lim and Hong* 2011], respectively. All of these schemes
143 predict the mixing ratios of water vapor, rain water, cloud water, cloud ice, snow and graupel.
144 The only exception is MY05, which also includes hail as a separate ice species. For convenience,
145 fast falling hail and graupel in MY05 are grouped together in the rest of this paper. The 1M
146 schemes use diagnostic relationships based on field measurements to derive the number
147 concentration of hydrometeors and their bulk fall speed. The 2M schemes predict the number
148 concentration of selected hydrometeor species, as summarized in Table 1. While most of them
149 have 2M treatment of both liquid and ice hydrometeors, the WDM6 2M scheme treats the
150 number concentration of ice phases as the WSM-1M scheme. In microphysical calculations
151 requiring droplet number concentration, it is fixed at 100 – 200 cm^{-3}, and heterogeneous ice
152 formation is treated diagnostically as specified variously within each scheme.
153 We use these different schemes to bracket the uncertainty in the microphysical schemes
154 since most were developed for mid-latitude application and have been calibrated only to a
155 limited extent for tropical applications (e.g., *Wu et al.* [2009], *Wang et al.* [2009], *Powell et al.*
156 [2012], *Del Genio et al.* [2012b], *Van Weverberg et al.* [2013], *Wu et al.* [2013]). At least two
157 advantages of 2M schemes have been noted in several studies of mid-latitude squall lines (e.g.,
158 *Morrison et al.* [2009], *Bryan and Morrison* [2012]). First, 2M schemes predicting rainwater
159 concentration can capture the transition from relatively large concentrations of rainwater in the

160 convective region to small concentrations in the stratiform region (the so-called "N_0 jump"
161 [*Waldvogel* 1974], while 1M schemes underestimate trailing stratiform precipitation due to
162 excessive evaporation of small rain droplets. Second, 2M schemes better represent the size
163 sorting process [*Milbrandt and Yau* 2005]. As shown below, 2M schemes can also better
164 reproduce observed radiation anomalies in stratiform areas.

165 Radiative fluxes are parameterized using the Goddard shortwave (SW) scheme [*Chou et*
166 *al.* 1999; *Matsui et al.* 2007; *Shi et al.* 2010] and the RRTMG longwave (LW) scheme [*Iacono et*
167 *al.* 2008], respectively. Hydrometeor mass and size distributions predicted or diagnosed by the
168 microphysics schemes are needed for precise computations of radiative fluxes. The computations
169 also require assumptions regarding crystal component aspect ratio and crystal distortion for ice
170 hydrometeors (e.g., van *Diedenhoven et al.* [2014]), parameters that are commonly undefined in
171 bulk microphysics schemes. By default, the effect of hydrometeor size is independent of
172 microphysical assumptions in the calculation of radiative transfer. For the SW radiative fluxes,
173 effective particle size is either a constant or a linear function of temperature by hydrometeor type.
174 For the LW fluxes, fixed effective radii of cloud water (5 μm), ice (10 μm), and snow (10 μm)
175 are used in 5 of the 6 microphysical schemes. The only exception is the Thompson scheme,
176 which is coupled with radiation through effective radii computed in the microphysics. The effect
177 of graupel is not taken into account in the LW radiation scheme.

178 The two-dimensional Smagorinsky first-order closure scheme is applied in physical space
179 to parameterize the horizontal transports by sub-grid scale eddies. The YSU first-order closure
180 scheme is adopted to parameterize boundary layer turbulence and vertical subgrid-scale eddy
181 diffusion [*Hong and Pan* 1996; *Noh et al.* 2003; *Hong et al.* 2006]. The implicit damping vertical
182 velocity scheme [*Klemp et al.* 2008] is used in the top 5 km of the computational domain to

183 suppress unphysical gravity wave reflection off the top boundary. These numerical options are
184 also used in *Wang et al.* [2013] to perform simulations of rain rates in the tropical ocean.
185 The computational domain has a dimension of 256x256x23 km^3. The lateral boundary is
186 doubly periodic, as in many other similar studies. The horizontal grid spacing is 1 km. A total of
187 60 stretched vertical levels are used with 10 levels in the first 1 km. We choose the numerical
188 options based on their conservation properties from our prior idealized tests with the WRF model
189 [*Wang and Sobel*, 2011, 2012, *Anber et al.* 2014]. We use a Coriolis parameter $f = 0$ in the
190 dynamics since the northern sounding array is very close to the equator. The incoming solar
191 radiation at the top of the atmosphere (TOA) at 76° E, 3°N is adopted uniformly over the domain
192 for the calculation of SW radiation. To reduce accumulated bias in column-integrated variables,
193 numerical experiments are reinitialized every 7 days. Model simulation from the first day is
194 considered to be the spin-up period, and discarded.
195 Simulated radar reflectivity, Z_e, is computed by integrating the size distributions for each
196 hydrometeor species (cloud water and cloud ice are neglected since their contribution for 10 cm
197 radar is negligible) based on Rayleigh scattering, while Mie scattering is neglected [*Smith* 1984,
198 *Blahak* 2007]. This is justified since we are comparing with 10-cm wavelength data from the S-
199 Polka radar.
200 **2.3 Observational data**
201 We use the following observational datasets to evaluate our numerical simulations. The
202 DYNAMO sounding array data [*Johnson and Ciesielski* 2013; *Ciesielski et al.* 2014] is used for
203 comparison with bulk meteorological quantities. Statistics of model-simulated radar echoes are
204 compared with the S-Polka radar reflectivity dataset from the University of Washington [*Powell*
205 *and Houze* 2013, *Zuluaga and Houze* 2013]. Large-scale mean surface fluxes are compared with

206 the 1-degree daily OAFlux data (Objectively analyzed air-sea Fluxes for Global Oceans, *Yu et al*.,
207 [2008]). Vertical profiles of radiative heating rates derived from the Combined Retrieval
208 algorithm (CombRet, *Comstock et al.* [2013]) are used as a reference. The CombRet retrieval
209 product is based on observations collected by merging S-PolKa and vertically pointing cloud
210 radar-lidar instruments located on Gan Island to account for both precipitating and non-
211 precipitating hydrometeor species [*Feng et al.*, 2014]. The cloud properties are used as input to a
212 radiative transfer model [*Fu and Liou* 1992; *Fu* 1996] to derive the radiative heating rates, and
213 surface and top-of-atmosphere fluxes.
214 The computed TOA radiative fluxes are compared with the CERES SYN1deg daily
215 radiative fluxes (Clouds and the Earth's Radiant Energy System, *Wielicki et al.* [1996]; *Loeb et*
216 *al*. [2012]) and with hourly 4-km broadband radiation fluxes from the Feng Yun (FY-2E)
217 geostationary satellite [*Minnis et al.* 2008]. The latter were initially determined from the FY-2E
218 visible (0.65 μm) and infrared (10.8 μm) radiances using the SW and LW, respectively,
219 conversion formulae determined from matched CERES and Multifunctional Transport Satellite
220 data [*Khaiyer et al.* 2010]. Because of calibration issues [*Minnis et al.* 2008], the resulting fluxes
221 required adjustment to more accurately represent the actual broadband data. On average, the
222 original FY-2E LW and SW fluxes were biased by 5.1% and -9.0%, respectively. The
223 corresponding standard deviations of the regional differences were 8% and 25%. Corrections
224 were developed by fitting 1° averaged FY-2E SW albedos and LW fluxes matched temporally
225 and spatially with their corresponding CERES Aqua SYN1 values to fourth and sixth order
226 polynomials for October, November, and December separately. The corrections yield unbiased
227 regional LW fluxes and SW albedos with instantaneous uncertainties of 4.2% and 13.1%,

228 respectively. The reflected SW (RSW) fluxes are the product of the albedos and solar-zenith-
229 angle corrected solar constant.

230 The S-Polka was located at Addu Atoll (0.63° S, 73.17° E) in the southwestern corner of
231 the NSA. The times of the peak MJO active phases based on radar-retrieved rain rate lead those
232 based on the large-scale spatial mean rainfall derived at the NSA by a few days. The mean rain
233 rate at 2.5 km determined from S-Polka data is ~6.6 mm/day, while the mean rain rate in the
234 NSA is ~9 mm/day based on both TRMM and derived rainrates. Because of this geographical
235 inconsistency, the time series of model simulations cannot be directly compared against S-Polka.
236 Instead, we will compare the histograms of radar reflectivity against observations by taking three
237 factors into account: rain rate, time sampling, and spatial sampling. First, the count of simulated
238 radar reflectivity is increased by 24 since the model simulation output is saved every 6 hours
239 while the S-Polka data are available every ~15 minutes. Second, model-simulated radar
240 reflectivity is reduced by the rain rate ratio between S-PolKa and NSA (i.e., 6.6 /9). A third
241 factor is the area ratio of the model and radar domains, since model output is subsampled to 2 km
242 to match the S-Polka data, which are re-gridded onto Cartesian coordinates at a horizontal
243 resolution of 2 km and vertical resolution of 0.5 km. This procedure allows us to rescale model-
244 simulated number of radar echoes for meaningful direct comparisons with radar data, but one
245 should also keep in mind that this is different from common practice to derive rain rates from Z
246 using empirical power-law (Z-R) relationship.

247 For the validation of three-dimensional cloud fields over the entire NSA domain, we also
248 use satellite image data for an indirect comparison of cloudiness. Brightness temperature (Tb)
249 data from the Meteosat Visible and InfraRed Imager (MVIRI) on board Meteosat-7 are available
250 every 30 minutes at a 5-km resolution in the water vapor (5.7 - 7.1 μm) and thermal infrared

(10.5 - 12.5 μm) bands. To derive Tb at these bands from the model data, we use the Radiative Transfer for TOVS (RTTOV, version 11.2, *Saunders et al.* [1999]) as the observation operator. The following data are used as input to RTTOV: sea surface temperature, vertical profiles of temperature and humidity, and the cloud fields, including the cloud fraction, cloud content, and cloud type. Because the numerical model has finer grid spacing than the satellite data, we compute cloud fraction as the percentage of cloud points within a 5x5 km^2 patch in the model domain, which has the same size as individual pixels from Meteosat-7. The Baron scheme is used for ice particle optical parameters based on temperature and ice water content. The RRTOV model has been validated using a highly accurate line-by-line radiative transfer model, and the bias for MVIRI is less than 1 K in the both bands (e.g., Table 13 in the Science and Validation Report of RTTOV-7).

3. Results

3.1 Surface rainrates and column integrated variables

As the large-scale vertical velocity and horizontal advection are prescribed in these simulations, surface rain rates are constrained to match observations to the first order. Figure 2 shows the time series of surface rain rates from all these simulations. As expected, the simulated values during the two simulated MJO active phases compare well with the budget derived values (black) and the areal average values from the TRMM data (gray). From the end of October to the beginning of November, there is also a notable discrepancy between model and TRMM results, which is likely due to the forcing being less accurate during that period when R/V Revelle was off station. Surface turbulent fluxes (sensible and latent heat fluxes), on the other hand, are less

273 well constrained by observations. CRM simulated surface fluxes are higher than observation
274 values, in general, and particularly during the convective phases.

275 Figure 3 compares time series of column-integrated and domain-averaged moist static
276 energy, dry static energy, precipitable water and column relative humidity with sounding array
277 observations. While the overall time evolution is reasonably well simulated in these experiments,
278 similar biases are present for all microphysics schemes, suggesting that uncertainty in the bulk
279 microphysical schemes is likely not responsible. In particular, dry static energy (DSE) does not
280 maintain nearly constant values but shows greater variability than that seen in observations. The
281 DSE is underestimated by the model for the first 2 weeks by all 6 microphysics schemes, and
282 then overestimated from day 17 to day 38, during the October MJO active phase. On the other
283 hand, the spread in the biases among the various microphysics results during most of the
284 remaining period (e.g., during day 21-33, 50 – 55) suggests that some of the error may be
285 attributed to particular microphysical schemes. For example, the MY05 scheme tends to produce
286 the greatest values of DSE and MSE, while the Thompson technique yields the greatest levels of
287 precipitable water. Overall, the differences among the microphysics schemes are relatively small,
288 particularly during minima in precipitable water when fewer clouds are likely present. In
289 addition, the model simulations using any of the microphysics schemes are similar in that they
290 consistently overestimate PWV, MSE and DSE. Our limited tests with revised subgrid eddy
291 viscosity shows reduced PWV in better agreement with observations, but the cloud fields are
292 insensitive to changes in eddy viscosity.

293 **3.2 Radiative fluxes**

294 Time series of the TOA radiation fluxes from CERES/SYN1deg are displayed in Figure
295 4a. The outgoing LW radiation (OLR) in Figure 4a exceeds 250 W/m^2 during the first two weeks

296 of the suppressed MJO phases, gradually dropping to 150 W/m^2 by the end of October and even
297 lower during the active phase of the November MJO (e.g., 125 W/m^2 around November 25).
298 Because of high reflectivity from deep convection and associated clouds, RSW (Figure 4b)
299 increases substantially during the two active periods, from 50 W/m^2 in the non-precipitating sky
300 to 200 W/m^2 during the last 10 days of November. As expected, RSW is more variable during
301 active periods owing to albedo dependence on cloud microphysics (e.g., liquid and ice content),
302 whereas OLR is less variable owing to its dependence on cloud top temperature. In principle,
303 cloud albedo also has a strong dependence on the sizes of liquid hydrometeors (e.g., Figure 3.14
304 of *Hartmann* [1994]), but the Goddard shortwave radiation code implemented in WRF uses fixed
305 effective hydrometeor sizes (see section 2.2); hence the difference in RSW can only be attributed
306 to the hydrometeor mass distribution.

307 The use of different microphysics schemes produces a large spread of radiative flux
308 biases in both OLR and RSW. Schemes that produce greater OLR anomalies also produce
309 greater RSW anomalies. There are also some systematic differences between the 1M and 2M
310 schemes, which are quite well separated with one exception, WDM6, which has nearly identical
311 ice processes as the 1M scheme, WSM6. The 1M schemes tend to underestimate radiative
312 anomalies by ~30 W/m^2 in the active phase, while the 2M schemes either underestimate or
313 overestimate these variables. For example, the MY05 simulation with the largest amount of snow
314 (as shown below) has absolute OLR and RSW biases exceeding 50 W/m^2 for much of the two
315 active phases. The column net radiation, defined here as the TOA and surface radiation flux
316 divergence (Figure 4c), indicates that two 2M schemes (Morrison and Thompson), on average,
317 produce column net radiation values that are comparable to their CERES counterparts and track
318 the CERES fluxes fairly closely during both active and suppressed phases.

319 During the active phase, reduced radiative cooling is a significant source of moist static
320 energy. The observed anomaly in column-integrated radiative cooling is more than 50 W/m^2
321 during the October active phases and nearly 100 W/m^2 in the end of November. The total
322 radiative heating even becomes positive for a few days (e.g., 25 November). The schemes that
323 simulate weak OLR and RSW anomalies (the 1M schemes and WDM6) have less variability.
324 The time mean radiation from CERES is -72.9 W/m^2 (Figure 4c). Morrison (-71.5 W/m^2) and
325 Thompson (-79.8 W/m^2) produce the best agreement with CERES, while the schemes that do not
326 simulate sufficient ice hydrometeors cool the atmosphere by an additional 20 W/m^2 or so (PLin, -
327 98.3, WSM6, -95.5, WDM6, -93.8). The MY05 method is consistently too high, exceeding
328 CERES by an average of 14 W/m^2.
329 Figure 5 shows time averaged radiative heating profiles from all the experiments. There
330 are no in-situ measurements of radiative heating profiles available. For reference, the net heating
331 rates for all sky conditions at Gan Island (the southwest corner of NSA) from CombRet are
332 shown in black. All the simulations agree to some extent in the lower part of the troposphere
333 with a cooling rate of ~1 K/day, similar to CombRet. However, close to surface, all the
334 simulations have a cooling rate of ~1 K/day, while CombRet has a cooling rate of ~ -2 K/day.
335 The simulated radiative heating rate also diverges in the upper troposphere. The two 1M schemes
336 and the WDM6 have cooling rates less than 1.5 K/day from 500 hPa to 200 hPa, while the
337 remaining 2M schemes cool the upper troposphere less due to abundant ice phase hydrometeors
338 (as discussed below). The micropulse lidar used in the CombRet underestimates the presence of
339 clouds in the upper troposphere during daylight hours due to the strong solar background sign.
340 This reduced sensitivity of signals with range and blocking by lower level clouds might
341 contribute to the underestimation of the net radiative cooling by CombRet compared to CERES

342 (averaged within 3x3° average over box centered at Gan) by more than 10 W/m^2 during the
343 whole period (not shown). This large discrepancy is also likely caused by the difference in
344 surface properties assumed in the radiative transfer model. CombRet assumes land surface,
345 which decreases the upwelling surface flux by 10 W/m^2 decrease compared to assuming an
346 ocean surface. The uncertainty in net cloud radiative effect due to upper tropospheric ice clouds
347 is ~1 K/day for CombRet compared to other retrieval algorithms [*Comstock et al.* 2013]. Finally,
348 none of the microphysics schemes has the peak cooling rate at ~ 580 hPa seen in CombRet. The
349 presence of this peak can be attributed to a sudden increase of liquid water content just below the
350 melting layer. Because of the difficulty in accurately retrieving mixed phase clouds within that
351 thin layer [*Feng et al.* 2014], the absence of this peak does not necessarily constitute a major
352 flaw of the models.

353 **3.3 Cloud fields**

354 In this section, we discuss the distribution of the cloud fields in space and time. Figure 6a
355 shows daily cloud area fraction as a function of height and time from CombRet, defined as the
356 ratio between the number of cloudy points (sum of ice water content and liquid water content
357 greater than 0.005 g/kg) and the number (2880) of observations over a day. The cloud fraction
358 over Gan is a few days ahead of NSA. All simulations (Figure 6 b-g) show the abrupt onset of
359 deep clouds immediately before both MJO active phases. The transition from shallow convection
360 to deep convection, normally expected to accompany the onset of the MJO active phase, is not
361 obvious, for example, on 1-2 day time scale (e.g., *Hagos et al.* [2014]). In addition to clouds
362 associated with the MJO, synoptic variability due to transients is also evident. For example, two
363 cloud episodes occurred during the suppressed MJO phases: upper level cloud at day 2-4 with
364 anomalous OLR up to ~-50 W/m^2 in model simulations but smaller in the observations (Figure

365 4a), and deep clouds around day 40 (~Nov 10). There are also some notable differences in the
366 clouds resulting from the microphysics schemes. In the active MJO phases, the 1M schemes
367 simulate much less cloudiness than the 2M schemes except for WDM6, which has a 1M
368 treatment of ice hydrometeors.

369 Brightness temperature, Tb, derived from the simulated cloud fields is shown in Figure 7
370 for in both IR and WV bands (Tb-IR and TB-WV, respectively). To the extent that the forward
371 radiative transfer model is accurate, differences between the model and satellite values, discussed
372 below, are attributed to uncertainties in the amount of cloud hydrometeors simulated by the
373 microphysics schemes and the assumed size distribution. There is overall agreement in the
374 temporal evolution of domain averaged Tb between model simulations and Meteosat-7. On the
375 other hand, uncertainty associated with cloud physics is evident in the two MJO active phases.
376 The mismatch between satellite and model simulations during the first week of November is also
377 evident, which is line with the rain rate (Figure 2a) and radiation (Figure 4) biases during that
378 period.

379 Values of Tb-IR (Figure 7a) are ~ 240-250 K during the last 10 days of October, and less
380 than 240 K during the last 10 days in November. Model simulated Tb-IR values have a spread of
381 more than 50 K, ranging from 220 K (PLin) to 280 K (MY05) during the first active phase, and
382 from 220 K to 260 K during the second. The time averaged Tb-IR from the Morrison scheme,
383 269.9 K, agrees best with satellite mean of 267.8 K. In the water vapor band, nearly all the
384 schemes systematic underestimate Tb-WV from the satellite (Figure 7b) during the suppressed
385 phases (e.g., October 1-15, November 1- 20). The Tb-IR histograms (Figure 7c) show a peak at
386 ~290 K for both the model and satellite data, while the Tb-WV histogram (Figure 7d) for the
387 satellite peaks at 243 K, ~ 2-3 K higher than all the model simulations. Very few values of Tb-

388 WV $\geq$ 243K were even simulated by the models. The bias in WV is consistent with the bias in
389 precipitable water (Figure 3c).
390 Figure 8a shows simulated domain mean profiles averaged over the entire period of
391 liquid water content (LWC), compared with LWC from Combret [*Feng et al.* 2014], which has
392 an uncertainty of ~20 – 30% for non-precipitating liquid clouds. While the uncertainty of LWC
393 at Gan is not provided (no independent LWC measurements are available), the cloud radar
394 dataset has been corrected for liquid attenuation and agrees well with the well-calibrated and
395 collocated S-Polka data (Fig. 12 in *Feng et al.* 2014).The reflectivity-rainrate (Z-R) relationship
396 used for rain water content retrieval is derived from in-situ surface disdrometer data [*Feng et al.*
397 2014].
398 The main difference between the simulations and CombRet is rainwater. CombRet
399 retrieves rainwater about 0.1-015 g/kg while all the model simulations simulate only less than
400 0.05 g/kg. Further analysis indicates that CombRet has abundant occurrences of rainwater
401 content greater than 1 g/kg, while values this large are rare in the model simulations. The
402 agreement between model simulations and CombRet is much better if time mean vertical profiles
403 of rainwater are computed without large rainwater (not shown), e.g., excluding values of
404 rainwater > 1 g/kg. Vertical profiles of rain water also differ from the model simulations in their
405 shape. Rain from CombRet decreases with height, while PLin-1M, WSM and Morrison produce
406 nearly uniform vertical distributions of total LWC. In MY05 and WDM6, LWC increases with
407 height, as CombRet. For rainwater, there is no evident separation between these 1M and 2M
408 schemes. The spread in rainwater content suggests large uncertainty in the rainwater
409 parameterizations in the various microphysics schemes, which may affect cold pool formation
410 (e.g., *Hagos et al.* [2014b] and *Feng et al.* [2015]).

411 Time mean vertical profiles of ice hydrometeors are shown in the right column of Figure
412 8. CombRet is again used for reference (its uncertainty is 20-30% for non-precipitating clouds
413 but unclear in deep convection [*Comstock et al.* 2013]). CombRet shows a gradually increasing
414 amount of ice hydrometeors with decreasing altitude from the upper troposphere down to the
415 melting level. The shapes of the ice content profiles from these model simulations are
416 qualitatively consistent with the means from CombRet for all species. Quantitatively, the range
417 of ice mixing ratios concentration varies by nearly four-fold, from 0.02 to 0.08 g/kg. Overall,
418 WSM, WDM, and Morrison agree better with CombRet quantitatively. In contrast to the liquid
419 case, the 2M and 1M simulations are well separated in the amount of ice content for each species.
420 The PLin scheme simulates the smallest amount of total ice. WSM6 and WDM6, which use the
421 same diagnostic (1M) treatment of cloud ice hydrometeors, have nearly identical profiles of
422 cloud ice and very similar amounts of snow, and both produce more ice amounts than does PLin.
423 The three schemes with 2M treatment of cloud ice (Thompson, MY05, Morrison) simulate more
424 total ice, but the abundance may be due to either cloud ice or snow. Thompson gives an
425 exceedingly large amount of snow (more than 0.06 g/kg at 8 km) but very little cloud ice (less
426 than 0.002 g/kg at 12-14 km), indicating efficient conversion from ice to snow. Two factors may
427 be responsible for an exceedingly small amount of cloud ice [*Van Weverbert et al.* 2013]: (1)
428 Thompson requires 120% supersaturation for ice nucleation. (2) Thompson is much more
429 efficient in converting ice to snow due to a 5-times-smaller threshold value in the volume-
430 weighted mean diameter.
431 Analysis of microphysical properties using S-Polka by *Rowe and Houze* [2014] indicates
432 that snow (dry aggregate) and ice (non-oriented ice) are stacked in different layers but their
433 occurrence frequencies are comparable within mesoscale convective systems. Because model

434 simulated hydrometeors are not classified in the same way as those from the particle
435 identification algorithm used in *Rowe and Houze* [2014] are, it is very difficult to make a further
436 quantitative comparisons between observations and simulations. Here we will only discuss the
437 stacked vertical structure of the species. Morrison and MY05 both give a layered structure of
438 cloud ice overlying snow, similar to observations, with the latter simulating the most ice content
439 among all the schemes. For graupel, most schemes produce similar profiles of graupel that peak
440 at ~5 km as in the observations (Figure 5 of *Rowe and Houze* [2014]), with Thompson
441 simulating the lowest graupel content among all the schemes (0.01 g/kg) at ~ 5 km. A likely
442 reason for the reduced graupel in Thompson is that Thompson forms graupel only through snow-
443 cloud liquid collisions, while other graupel formation mechanisms are not considered (e.g.,
444 collision between rain and snow, and rain and snow). *Rowe and Houze* [2014] also showed that
445 occurrence of particles identified as graupel is one order of magnitude smaller than for dry
446 aggregate (snow). Thus it is possible that all the schemes could have overestimated graupel, as
447 found in other studies (e.g., *Varble et al.* [2011]), but it should be noted that domain-mean
448 occurrence frequency and domain-mean mass mixing ratio are different quantities, making it
449 impossible for direct comparison.

450 The large spread of ice species among these simulations having different microphysics
451 can generally be attributed to two factors: (1) their sources or sinks are treated very differently or
452 (2) sedimentation rates differ greatly. Fully exploring the differences in phase conversion is
453 difficult because it involves too many parameters in these highly nonlinear schemes. Here we
454 will address the sedimentation issue briefly. Intuitively, everything being equal, small terminal
455 speeds would favor build-up of hydrometeors. To see if this is useful to explain some of the
456 differences, Figure 9 shows the histogram of the fall speed as a function of height for the two

457 hydrometeors in which these simulations disagree the most: cloud ice and snow. The terminal
458 speeds of these two hydrometeor types have similar equations as well as some important
459 differences. For cloud ice, WSM6 and WDM6 have a relatively large fall speed (0.7 m/s) in all
460 layers and PLin has median values of 0.4-0.5 m/s in the ice-rich layer (9-12 km). MY05 and
461 MORR have relatively small fall speeds (less than 0.3 m/s) in their ice layers (denoted as black
462 curves). Thompson also has a low fall speed but its conversion to snow is efficient (as discussed
463 above). Thus, the schemes with 1M treatment of cloud ice have larger fall speeds compared with
464 2M treatments, consistent with greater accumulation from the 2M schemes.
465 The fall speed of large hydrometeors such as snow is generally larger than that of smaller
466 cloud ice particles (right column of Figure 9) as expected. Most schemes (except PLin) have fall
467 speed decreasing with height because of larger snow hydrometeors in the lower layers. PLin,
468 WSM6, and WDM6 all have relatively large fall speeds (> 0.8 m/s). Thompson and MY05 have
469 smaller fall speeds (~0.5m/s) in their snow layers. Morrison has relatively large snow fall speeds
470 (~1 m/s); thus fall speed cannot explain why its snow content is greater than its WDM6
471 counterpart.
472 Overall, greater terminal fall speed of cloud ice may in part explain why ice in 1M
473 schemes is generally less than in 2M schemes, with the exception of Thompson, which converts
474 ice to snow very efficiently. The same may be stated for snow, but also with the exception of one
475 scheme (Morrison). Due to the large number of parameters in each scheme, the microphysical
476 transformations are too complex to allow us to precisely identify the source of the discrepancy
477 within the scope of this work. Fall velocity retrieval is not available in CombRet at the time of
478 this study, but will be very useful to constrain the microphysics parameterizations given the large
479 range of variability in future studies.

480 **3.4 Radar reflectivity**

481 Convective and stratiform partitioning is an objective technique to analyze precipitating
482 clouds directly from observed radar reflectivity. Historically, this technique has been
483 instrumental in the development of fundamental understanding of stratiform processes (e.g.,
484 *Houze* [2009], *Schumacher and Houze* [2003]). The texture-based empirical algorithm applies
485 thresholds to values and area coverage of reflectivity within the lower troposphere to separate
486 active convective elements and stratiform clouds. The algorithm is not unique, and the exact
487 values of the thresholds vary to some extent in different studies because the algorithm needs to
488 be checked against vertical radar scans (*Steiner et al*. [1995], *Yuter* et al [1997]). Here we apply
489 the same threshold values used by *Powell and Houze* (2013] and *Zuluaga and Houze* [2013] to
490 model simulated radar reflectivity at 2.5 km and decompose them into stratiform and convective
491 categories for radar echoes greater than 5 dBz. To avoid inclusion of isolated shallow convection
492 as stratiform outflow in the simulation results, an additional constraint, used in *Fridlind et al.*
493 [2012], is also employed to better expose the relationship between the radar observations and
494 radiative fluxes: reflectivity must be at least 5 dBZ at 6 km elevation in stratiform columns.
495 Snapshots of the convective and stratiform separation of the S-Polka radar reflectivity at 10 UTC
496 11 November is shown in Figure 10 a and b**.**

497 Figure 11 shows time series of area fraction of the model-simulated stratiform and
498 convective echoes. These differ substantially from the S-Polka results because S-Polka only
499 samples a small portion of NSA. After the first two weeks of the suppressed period in October,
500 convective rain episodes begin to occur in multiple 2-day events. During the first few days of
501 this MJO active phase, the simulated stratiform rain only shows some moderate peaks associated
502 with these convective episodes while S-Polka shows substantial stratiform rain during the first

episode. Stratiform rain areal coverage in the simulations expands greatly after October 20. Thus stratiform peaks lag convective maxima by a few days. This lag is also seen during the November MJO: convective rain episodes start November 16, while stratiform fraction increases substantially after November 22, although the amount of stratiform fraction is clearly microphysics dependent. For example, the stratiform peaks range from less than 20% to more than 80%. *Zuluaga and Houze* [2013] analyzed S-Polka radar echoes by separating them into even more categories (e.g., shallow convective, deep convective, broad stratiform). They also demonstrated the lag of stratiform to convective rain in the radar echoes. *Sobel et al.* [2014] noted that the large-scale vertical velocity gradually becomes more top-heavy during later phases, probably associated with the changing form of the cloud population.

Substantial differences between the 1M and 2M schemes can be identified. Stratiform precipitation as simulated by most of the 2M schemes (except WDM6) covers nearly half of domain in the first active MJO phase, and more than half of the model domain in the second active phase. But the stratiform area fraction from the 1M schemes is less than 20% most of the time, coverage that is of the same magnitude as the convective area. In contrast, stratiform area fraction in the 2M schemes is nearly 3-5 times greater than convective fraction, similar to S-Polka. The difference between stratiform coverage in 1M versus 2M schemes is consistent with some earlier studies (e.g., *Morrison et al.* [2009], *Bryan and Morrison* [2011], *Hagos et al.* [2014]).

Figure 12 shows histograms of both convective and stratiform echoes at 2.5 km from the simulations along with those from the S-Polka data, where model-simulated values have been rescaled as stated in the last paragraph of Section 2.3. Although the 1M schemes match the observed convective rain reflectivity histogram shape quite well, most 2M schemes tend to

526 produce too many convective echo, similar to what other studies have found (e.g., Figure 8 of
527 *Varble et al.* [2011], *Fridlind et al.* [2012], *Hagos et al.* [2014]). The stratiform echoes from S-
528 Polka are evenly distributed below 20 dBz, while the simulated stratiform shows strong
529 dependence on the microphysical treatment of clouds. 2M schemes simulate more stratiform rain
530 echoes between 10 - 25 dBz with a distinct peak not seen in observations. Fewer stratiform
531 echoes for reflectivity less than 10 dBz are generated due to masking at 6 km height. Without
532 this masking, we would see more smaller-dBz echoes misclassified as stratiform in both
533 simulations and S-Polka data. Like the time series of stratiform echoes (Figure 11), the number
534 of stratiform echoes from 1M schemes is less than that from 2Ms. The two 1M schemes and one
535 2M (WDM6) simulate much less stratiform echo than does S-Polka.
536 Figure 12c shows the histogram of all radar reflectivities at the 6-km masking height,
537 (more than 1 km above the melting level), where snow and graupel are the dominant classes of
538 hydrometeors (Figures 4 and 5) in all these simulations. Overall, the systematic bias of the 2Ms
539 in low-level stratiform clouds is reduced compared with S-Polka, while the 1Ms still
540 underestimate that cloud type. S-Polka radar echoes are nearly uniformly distributed from -5 to
541 15 dBz with a peak at 0 dBz. All the 1M schemes simulate nearly half of the echo events of S-
542 Polka. The Morrison and Thompson-2M show better agreement with S-Polka at 6.5 km. The
543 2Ms (except WDM6) simulate more weak echoes (less than -10 dBz) than S-Polka.
544
545 **3.5 Relationship between radiative fluxes and radar reflectivity**
546 As shown above, both cloud and radiation fluxes vary substantially with these different schemes.
547 Since precipitation is approximately constrained by the large-scale forcing to match observation
548 while the cloud physics is not similarly constrained, cloud-radiative interaction is entirely subject

549 to uncertainties in the relevant model physics. Figure 13 summarizes a radiative feedback
550 parameter derived from observations and these simulations as the linear coefficient of column
551 net radiative heating and precipitation using a least squares second-order polynomial fit (in
552 contrast to linear regression, this taken into account of linear regression coefficient varying with
553 different rain ranges). Radiative feedback from TRMM and CERES is ~0.17 at 0 mm/day rain
554 rate, and drops to 0.14 at 15 mm/day, 0.12 at 30 mm/day. The simulations with 1M cloud water
555 and rain (PLin and WSM6) and cloud ice (WDM6) underestimate radiative feedback at these
556 rain rate ranges. On the other hand, the simulations with 2M schemes overestimate radiative
557 feedback, which decreases with the rain rates, similar to the observation. In this section we
558 explore in detail what could cause these variations in cloud-radiative interaction.
559 Figure 14 shows the scatter plot of mean ice water path (IWP, including any cloud ice,
560 snow, graupel and hail if extant) and liquid water path (LWP, including cloud water and
561 rainwater) versus average OLR and RSW. IWP varies in the range from 50 to 300 g/m^2, and a
562 reasonable linear correlation between IWP and OLR or RSW is evident. OLR from half of the
563 schemes is less than CERES OLR (gray vertical bar), while the other results are greater than the
564 CERES average. Simulations having more IWP (MY05, Morrison, Thompson) generally yield
565 smaller OLR (< 220 W/m^2) and greater RSW (> 110 W/m^2) values in the time mean. In contrast,
566 simulated time mean LWPs are within a narrower range, 10 to 20 g/m^2, despite OLR and RSW
567 varying significantly. The quasi-linear relationship between IWP and OLR or RSW may not be
568 surprising, given that the effective radius for the same species is the same in the radiation
569 computation, and optical thickness is a linear function of water content. This differs somewhat
570 from the findings of *Fridlind et al.* [2012], where most simulations varied little in IWP but

571 widely in OLR in a manner that was correlated with variation in the simulated stratiform area
572 over which the IWP was distributed.

573 Radiative fluxes are closely related both to the areal coverage of clouds and to cloud top
574 height. Here, we consider cloudy areas identified from 2.5 km radar echoes and total echo area
575 (for any grid points with echo greater than -30 dBz) at 6 km. Figure 15 shows that the stratiform
576 area and time-mean domain averaged OLR for the whole period are well correlated, and the
577 correlation is better overall when the echo at 6 km is used (right column of Figure 15). In either
578 case, the observations divide the plot into four quadrants, only two of which are occupied by
579 simulations owing to offsetting biases in OLR and echo or stratiform area fraction. We further
580 divide the data into two periods: the active phases 15 October– 2 November and 20 November –
581 1 December), and the suppressed phases (the remaining days). The relation between OLR and
582 the 2.5-km stratiform area fraction or 6-km echo area fraction remains nearly the same during the
583 active phase, with roughly half of the simulations overestimating OLR by 20-30 W/m^2
584 (underestimating cloud area and/or cloud-top height) and the other half underestimating OLR by
585 10-40 W/m^2 (overestimating cloud area and/or cloud-top height). In the suppressed phase,
586 however, the schemes with 2M treatment of cloud ice (MY05, Morrison, Thompson) still
587 underestimate OLR by 10-30 W/m^2 associated with ice clouds, whereas the rest (1M ice schemes)
588 show better agreement with observed OLR (within 5 W/m^2). It is possible that the use of doubly
589 periodic boundary conditions may be the cause of the overly persistent upper-level clouds during
590 the suppressed phases in the 2M simulations. Overall, 6-km echo area fraction and radiation
591 anomalies are better correlated than stratiform area fraction and radiation, indicating that the
592 variation of cloud vertical structure differs substantially in the 2M schemes.

593 To explore the relationships between RSW and stratiform and echo fractions, it is
594 necessary to examine the averages at the same time of day because of the strong diurnal cycle of
595 solar radiation. Using a single time of day reduces the sample size for each comparison. Here, we
596 examine the relationships at 1100 LT using averages from FY-2E observations. For TOA RSW
597 at noon time, Figure 16 shows that again 1M schemes are close to each other, indicating
598 systematic biases in cloud fraction and radiation, while other 2M schemes are well scattered. In
599 the active phase, it appears that the 1M schemes simulate reasonable cloud albedos, while the
600 Morrison and Thompson are better during the majority of periods when the MJO convection is
601 suppressed. MY05 has the most abundant cloud snow and is the most reflective among these
602 simulations, even though its stratiform area is not the most abundant. This comparison
603 demonstrates that increases in stratiform clouds are associated with decreases in column radiative
604 cooling (and lower OLR values). Echo area and reflectivity relationships are better exposed if 6
605 km radar reflectivity is used (left column) because of uncertainty in the vertical structure of
606 hydrometeors, especially during the suppressed phase.
607 Observed radar echoes can be used to divide the total sky into different regions. Here we
608 focus on two cloud regimes: (1) rainy area, where either a stratiform rain or convective rain
609 column can be identified, and (2) elsewhere, referred to as “non-precipitating” regions, including
610 weakly rainy area with dBz less than 5, cloudy sky, and completely cloud-free sky. We compare
611 the model simulated radiative fluxes at TOA with the 4-km FY-2E dataset. The FY-2E TOA
612 fluxes are collocated with the S-Polka radar if the image time is within a ±5 minute window. A
613 snapshot of such collocations is shown in Figure 10 c and d for 2000 UTC, 11 November 2011.
614 The cloudy area identified by radar echoes (stratiform and convective echoes) corresponds
615 reasonably well to low OLR values.

Figures 17 shows histograms of OLR (left column) and RSW (right column) over rainy, non-precipitating, and total skies. As shown in previous subsection on the time mean radiation anomalies (e.g., Figure 14), most simulated OLR spectra from the 2M schemes agree better with the observed one than do those from the 1M simulations. Figure 17a shows no systematic difference between 1M and 2M for OLR > 215 W/m^2 in rainy areas, but the 1Ms systematically underestimate OLR frequencies for OLR < 230 W/m^2. This can be contrasted with the overestimate of OLR < 135 W/m^2 occurrences in the 2M histograms, which is reflected in the greater frequencies of RSW > 800 W/m^2 in Figure 17d. The 1M schemes produce a stronger warm peak in non-precipitating areas (Figure 17b), but all of the simulations underestimate the frequency maximum by ~15 W/m^2. For non-precipitating areas, the frequencies of model OLR values for OLR between 150 and 250 W/m^2 are significantly underestimated and RSW occurrence (Figure 17e) is overestimated for RSW > ~750 W/m^2., and underestimated for RSW less than that value. The one exception is the MY05 scheme, which matches the observations for RSW < 550 W/m^2. The histograms for all-sky conditions (Figure 17c, f) combine the features of the precipitating and non-precipitating scenes and demonstrate that the differences between the models and the observations are present even if precipitation is not considered explicitly.

The OLR and RSW biases are most dramatic in deep convective regimes (Figure 17a, d) where model simulations have abundant cloud cover. Similar biases are also seen in the histogram of the brightness temperature (Figures 7c and d). The marked differences suggests that the 2M schemes generate far more deep convective cloud cover than is present and that perhaps the ice water content at the tops of the anvils is much too great. It is possible that the circulation within the model domain because of doubly periodic boundary conditions would cause an unrealistic increase in cloud optical depth, but similar biases in microphysics and dynamics have

639 been found across simulations with and without such boundary conditions owing to causes that
640 have not yet been clearly identified (*Varble et al.* [2014a, 2014b]).
641 Histograms of OLR and RSW in non-precipitating sky regions reveal some differences
642 between the model and satellite estimates. In the non-precipitating sky situations, the model--
643 simulated OLR peaks at 265 W/m^2 (Figure 17b**)**, while the FY-2E observations show a peak at
644 nearly 280 W/m^2. This 15 W/m^2 difference is outside of the FY-2E OLR uncertainty. The FY-2E
645 OLR is unbiased over the observed range (Section 2.3) so that the histogram extrema should not
646 be off set from the true value, assuming the instantaneous uncertainty of 4% (11.2 W/m^2 at 280
647 W/m^2) is randomly distributed about the mean. Histograms of 1° CERES OLR for all sky
648 conditions also indicates a peak of ~280 W/m^2 (not shown), similar to that from FY-2E. Thus,
649 these differences in warm frequency maxima are more likely due to the model atmospheres being
650 either too moist or generating more low-level cloud cover than is actually present, or the model
651 misses a diurnal cycle in heating of the ocean mixed layer. These possibilities are discussed
652 below.
653 Precipitable water is overestimated in the models by 10% (Figure 3). If the profile water
654 vapor is increased by 10%, radiative transfer calculations indicate a 2-3 W/m^2 decrease in OLR
655 for a clear scene. Adding a 20% low cloud cover with an optical depth of 5 and tops at 800 hPa
656 would produce a 7 W/m^2 drop in the OLR, while doubling the RSW. The underestimate of RSW
657 for RSW < 500 W/m^2 suggests that cloud-free skies occur less frequently than in reality. Thus,
658 the more frequent occurrence of scattered low clouds is likely to be significant contributor to the
659 frequency peak difference. The CRM simulations are driven by daily mean SST, but diurnal
660 warming in the mixed layer could cause SST to increase, on average, by ~0.5 - 1 K (e.g., *Kawai*
661 *and Wada* [2007], *Matthews et al.* [2014]) after noon in the suppressed phase, which would lead

662 to less than 1-2 W/m^2 underestimate by the models. This diurnal warming in SST is absent in our
663 simulations, but could also be incorporated using a skin temperature parameterization as *Wang et*
664 *al.* [2015]. Hence the simulated emission temperature and the clear-sky OLR could be lower than
665 observed values by ~1-2 W/m^2 in the suppressed MJO phases. It is likely that all of these factors
666 play some roles in the underestimation of OLR by the models for relatively cloud-free conditions.
667 Determining the relative contributions will require more detailed cloud and SST observations.
668
669 **4. Discussion and conclusions**
670 We have examined clouds and radiative fluxes in a set of cloud-resolving simulations of
671 two DYNAMO MJO events. The simulations are driven by the large scale forcing dataset from
672 the DYNAMO northern sounding array, and carried out in doubly-periodic domains using the
673 WRF model. Simulated cloud properties and radiative fluxes are compared to the observed
674 reflectivity from the S-Polka radar and observed radiative fluxes from the CERES and FY-2E
675 datasets. To accommodate the uncertainty in cloud microphysics, we have tested a number of
676 single moment (1M) and double moment (2M) microphysical schemes in the WRF model.
677 It is found that all the schemes using a 1M treatment of cloud ice species produce lower
678 ice contents than do the 2M schemes. Analysis of fall speed suggests that greater terminal fall
679 speed of both cloud ice and snow may in part explain this. While the microphysical
680 transformations are too complex to allow us to precisely identify the source of discrepancy with
681 the scope of this work, the identification of cloud and snow ice fall speeds as an important factor
682 points to the potential usefulness of comparing simulated and observed mean Doppler velocities
683 within widespread stratiform regions (cf. rain in Figure 8 of *Varble et al.* [2014b]).). Comparison
684 of simulated brightness temperatures with observations from Meteosat-7 confirms that the 1M

685 schemes systematically underestimate IR Tb during the active phase, while Tb values from the
686 2M schemes show a large spread and one of the 2M schemes agrees well with the satellite
687 observations. Tb values in the WV indicate that the 2M schemes are more capable of simulating
688 stronger Tb anomalies. However, interpretation of WV Tb is complicated by systematic biases
689 likely related to humidity biases across the simulations.

690 Time series of the simulated domain-averaged TOA radiative fluxes (OLR and RSW) are
691 compared against those from the CERES/SYN1deg data. Schemes that produce greater OLR
692 anomalies also produce greater RSW anomalies. The 1M schemes tend to underestimate
693 radiative flux anomalies in the active phases of the MJO, while the 2M schemes perform better
694 but can still overestimate radiative flux anomalies. Skill of the model simulations in capturing
695 the domain averaged TOA radiative fluxes is closely related to their skill in simulating stratiform
696 rain and non-precipitating cloud structures, which is in turn tied to the model treatment of cloud
697 physics. It is found that in general the 1M schemes tend to underestimate stratiform radar echo
698 area relative to the S-Polka radar data, while the schemes with the 2M treatment of ice species
699 simulate too much stratiform echo coverage. For convective echoes, the 1M schemes perform
700 better than the 2Ms which give too many convective echoes. However, this is less consequential
701 for the radiative fluxes since expansive optically thick stratiform echoes are much more
702 important for radiation than convective echoes. At upper levels, time evolution of radar echoes
703 and their histogram shows systematic low bias for 1M simulated echoes, while the stratiform
704 echo bias in the 2M schemes is reduced.

705 The accuracy of the simulated TOA radiative flux is further assessed by conditioning of
706 radiative fluxes upon the radar echoes and dividing the full sky into precipitating and non-
707 precipitating areas. While time series of radiative fluxes from certain microphysics schemes

708 track observations well, histograms of radiative fluxes over both precipitating and non-
709 precipitating areas exhibit systematic biases. A fat tail in the OLR distribution is seen in the rainy
710 area for OLR less than 150 W/m^2 in the schemes with 2M treatment of cloud ice, and the
711 opposite is seen in all the 1M schemes. Simulated OLR in the non-precipitating sky situations
712 peaks at 265 W/m^2, which is about 15 W/m^2 smaller than the FY-2E maximum frequency,
713 indicating the need for better treatment of some of the model components, humidity, low cloud
714 formation, and diurnal variations of SST.

715 Accurate modeling of the cloud fields is essential for correct simulation of the radiation
716 fields. A further detailed analysis of cloud microphysics and its fine tuning using the DYNAMO
717 microphysics observations [*Rowe and Houze* 2014, *Barnes and Houze* 2014] will be an
718 important next step for future model improvement.

719

720 **Acknowledgments**

721 SW and AHS were supported by NSF grant NSF AGS-1062206. We thank Mr. Scott Powell and
722 Manuel Zuluaga for their clarification of the convective/stratiform analysis, Hannah Barnes for
723 the discussion on the observed microphysical structures. The CERES-SYN1deg data were
724 provided by the CERES team via their webpage:
725 http://ceres.larc.nasa.gov/products.php?product=SYN1deg. Thanks to R. Palikonda and M.
726 Khaiyer for assistance in the analysis of FY-2E data, which was supported by the Department of
727 Energy Atmospheric Science Research Program under Interagency Agreement DE-
728 SC0000991/006. The Combined Retrieval Data were obtained from the Atmospheric Radiation
729 Measurement (ARM) Program sponsored by the U.S. Department of Energy, Office of Science,
730 Office of Biological and Environmental Research, Climate and Environmental Sciences Division.

Reference

Anber, U., Wang, S., and A. H. Sobel (2013), Response of Atmospheric Convection to Vertical Wind Shear: Cloud Resolving Simulations with Parameterized Large-Scale Circulation. Part I: Specified Radiative Cooling. *Journal of the Atmospheric Sciences.* **71**, 2976–2993.

Andersen, J. A. and Z. Kuang, 2011: Moist static energy budget of MJO-like disturbances in the atmosphere of a zonally symmetric aquaplanet. J. Climate, 25, 2782–2804, doi:10.1175/JCLI-D-11-00168.1.

Barnes, H. C., and R. A. Houze, Jr., 2014: Precipitation hydrometeor type relative to the mesoscale airflow in oceanic deep convection of the Madden-Julian Oscillation. *J. Geophys. Res. Atmos.,* in review.

Bessafi, M., M. C. Wheeler, 2006: Modulation of South Indian Ocean Tropical Cyclones by the Madden–Julian Oscillation and Convectively Coupled Equatorial Waves. *Mon. Wea. Rev.*, **134**, 638–656.

Blahak, U., 2007: RADAR_MIE_LM and RADAR_MIELIB—Calculation of radar reflectivity from model output. Internal Rep., Institute for Meteorology and Climate Research, University/Research Center Karlsruhe, 150 pp.

Blossey, P. N., C. S. Bretherton, J. Cetrone, and M. Khairoutdinov, 2007: Cloud-resolving model simulations of KWAJEX: Model sensitivities and comparisons with satellite and radar observations. *J. Atmos. Sci.*, **64**, 1488-1508.

Bony, S., and K. A. Emanuel, 2005: On the Role of Moist Processes in Tropical Intraseasonal Variability: Cloud–Radiation and Moisture–Convection Feedbacks. *J. Atmos. Sci.*, **62**, 2770–2789.

Bryan, G. H. and H. Morrison, 2012: Sensitivity of a Simulated Squall Line to Horizontal Resolution and Parameterization of Microphysics.*Mon. Wea. Rev.*, **140**, 202–225.

Camargo, Suzana J., Matthew C. Wheeler, Adam H. Sobel, 2009: Diagnosis of the MJO Modulation of Tropical Cyclogenesis Using an Empirical Index. *J. Atmos. Sci.*, **66**, 3061–3074.

Cassou, C. (2008), Intraseasonal interaction between the Madden-Julian Oscillation and the North Atlantic Oscillation, *Nature*, ***455***, 523–527.

Ciesielski, P. E., and Coauthors, 2014: Quality-Controlled Upper-Air Sounding Dataset for DYNAMO/CINDY/AMIE: Development and Corrections.*J. Atmos. Oceanic Technol.*, **31**, 741–764.

Chen, S-H., and W-Y. Sun, 2002: A one-dimensional time dependent cloud model. *J. Meteor. Soc. Japan*, **80,** 99–118.

Chikira, M., 2014: Eastward-Propagating Intraseasonal Oscillation Represented by Chikira–Sugiyama Cumulus Parameterization. Part II: Understanding Moisture Variation under Weak Temperature Gradient Balance. *J. Atmos. Sci.*, **71**, 615–639.

Chou M.-D., and M. J. Suarez, 1999: A solar radiation parameterization for atmospheric studies. NASA Tech. Rep. NASA/TM-1999-10460, vol. 15, 38 pp

770 Comstock, J. M., A. Protat, S. A. McFarlane, J. Delanoë, and M. Deng (2013), Assessment of
771 uncertainty in cloud radiative effects and heating rates through retrieval algorithm differences:
772 Analysis using 3 years of ARM data at Darwin, Australia, *J. Geophys. Res. Atmos.*, 118(10),
773 4549-4571, doi:10.1002/jgrd.50404.

774 Del Genio, A.D., Y.-H. Chen, D. Kim, and M.-S. Yao, 2012a: The MJO transition from shallow
775 to deep convection in CloudSat/CALIPSO data and GISS GCM simulations. *J. Climate*, **25**,
776 3755-3770, doi:10.1175/JCLI-D-11-00384.1.

777 Del Genio, A.D., J. Wu, and Y.-H. Chen, 2012b: Characteristics of mesoscale organization in
778 WRF simulations of convection during TWP-ICE. *J. Climate*, **25**, 5666-5688, doi:10.1175/JCLI-
779 D-11-00422.1.

780 DePasquale, A., C. Schumacher, and A. Rapp, 2014: Radar observations of MJO and Kelvin
781 wave interactions during DYNAMO/CINDY2011/AMIE. *J. Geophys. Res*., **119**,
782 doi:10.1002/2013JD021031.

783 Feng, Z., S. A. McFarlane, C. Schumacher, S. Ellis, and N. Bharadwaj, 2014: Constructing a
784 merged cloud-precipitation radar dataset for tropical clouds during the DYNAMO/AMIE
785 experiment on Addu Atoll. *J. Atmos. Oceanic Technol.*, 31, 1021–1042.

786 Feng, Z., S. Hagos, A. K. Rowe, C. D. Burleyson, M. N. Martini, and S. P. de Szoeke (2015),
787 Mechanisms of convective cloud organization by cold pools over tropical warm ocean during the
788 AMIE/DYNAMO field campaign, *J. Adv. Model. Earth Syst.*, in press,
789 doi:10.1002/2014ms000384.

790 Fridlind, A. M., et al. (2012), A comparison of TWP-ICE observational data with cloud-
791 resolving model results, *J. Geophys. Res.*, 117, D05204, doi:10.1029/2011JD016595.

792 Fu, X., and B. Wang, 2009: Critical Roles of the Stratiform Rainfall in Sustaining the Madden-
793 Julian Oscillation: GCM Experiments. *J. Climate*, **22** , 3939-3959. Fu, Q., and K. N. Liou, 1992:
794 On the correlated k-distribution method for radiative transfer in nonhomogeneous atmospheres. J.
795 Atmos. Sci., 49, 2139-2156

796 Fu, Q., 1996: An accurate parameterization of the solar radiative properties of cirrus clouds for
797 climate models. *J. Climate*, 9, 2058-2082.

798 Fuchs, Z., and D. J. Raymond, 2002: Large-scale modes of a nonrotating atmosphere with water
799 vapor and cloud-radiation feedbacks. *J. Atmos. Sci.*, 59, 1669-1679.

800 Garfinkel, C. I., S. B. Feldstein, D. W. Waugh, C. Yoo, and S. Lee (2012), Observed connection
801 between stratospheric sudden warmings and the Madden-Julian Oscillation, *Geophys. Res.*
802 *Lett.,* **39**, L18807, doi:10.1029/2012GL053144.

803 Gottschalck, J., P. Roundy, C. Schreck, A. Vintzileos, and C. Zhang, 2013: Large Scale
804 Atmospheric and Oceanic Conditions During the 2011-2012 DYNAMO Field Campaign. *Mon.*
805 *Wea. Rev.,* **141**, 4173–4196. doi:10.1175/MWR-D-13-00022.1

806 Grabowski, W. W., X. Wu, and M. W. Moncrieff (1996), Cloud resolving modeling of tropical
807 cloud systems during Phase III of GATE. Part I: Two-dimensional experiments, *J. Atmos. Sci.,*
808 *53*, 3684-3709.

809 Hagos, S., Z. Feng, K. Landu, and C. N. Long (2014a), Advection, moistening, and shallow-to-
810 deep convection transitions during the initiation and propagation of Madden-Julian Oscillation, *J.*
811 *Adv. Model. Earth Syst.*, *6*(3), 938-949, doi:Doi 10.1002/2014ms000335.

812 Hagos, S., Z. Feng, C. D. Burleyson, K.-S. S. Lim, C. N. Long, D. Wu, and G. Thompson
813 (2014b), Evaluation of convection-permitting model simulations of cloud populations associated
814 with the Madden-Julian Oscillation using data collected during the AMIE/DYNAMO field
815 campaign, *J. Geophys. Res. Atmos.*, *119*(21), 2014JD022143, doi:10.1002/2014JD022143.

816 Hall, J., A. J. Matthews, and D. Karoly, 2001: The modulation of tropical cyclone activity in the
817 Australian region by the Madden–Julian oscillation. *Mon. Wea. Rev,* **129**,2970–2982.

818 Hartmann, D.L., 1994, Global Physical Climatology. **55.** *International Geophysics*. Academic
819 Press.

820 Hong, S. Y., and H. L. Pan ,1996, Nonlocal boundary layer vertical diffusion in a Medium-
821 Range Forecast model, Mon. Weather Rev., 124, 2322–2339.

822 Hong, S.-Y., Y. Noh, and J. Dudhia (2006), A new vertical diffusion package with an explicit
823 treatment of entrainment processes, *Mon. Wea. Rev.*, *134*, 2318–2341.

824 Hong, S-Y., and J-O. J. Lim, 2006: The WRF single-moment 6-class microphysics scheme
825 (WSM6). *J. Korean Meteor. Soc.*, **42,** 129–151.

826 Huang, P., C. Chou, R. Huang, 2011: Seasonal Modulation of Tropical Intraseasonal Oscillations
827 on Tropical Cyclone Geneses in the Western North Pacific. *J. Climate*, **24**, 6339–6352.

828 Hung, M-P., J.-L. Lin, W. Wang, D. Kim, T. Shinoda, and S. J. Weaver, 2013: MJO and
829 Convectively Coupled Equatorial Waves Simulated by CMIP5 Climate Models. *J. Climate*, **26**,
830 6185–6214.

831 Iacono, M.J., J.S. Delamere, E.J. Mlawer, M.W. Shephard, S.A. Clough, and W.D. Collins,
832 Radiative forcing by long-lived greenhouse gases: Calculations with the AER radiative transfer
833 models, *J. Geophys. Res.*, **113**, D13103, doi:10.1029/2008JD009944, 2008.

834 Janiga, M., and C. Zhang (2015): MJO Moisture Budget during DYNAMO in a Cloud-
835 Permitting Model. J. Atmos. Sci. In review.

836 Johnson, R. H., and P. E. Ciesielski, 2000: Rainfall and Radiative Heating Rates from TOGA
837 COARE Atmospheric Budgets. *J. Atmos. Sci.*,**57**, 1497–1514.

838 Johnson, R. H., and P. E. Ciesielski, 2013: Structure and Properties of Madden–Julian
839 Oscillations Deduced from DYNAMO Sounding Arrays. *J. Atmos. Sci.*, **70**, 3157–3179.

840 Johnson, R. H., P. E. Ciesielski, J. H. Ruppert, and M. Katsumata (2015), Sounding-Based
841 Thermodynamic Budgets for DYNAMO, *J. Atmos. Sci.*, *72*(2), 598-622, doi:10.1175/jas-d-14-
842 0202.1.

843 Jones, C., 2000: Occurrence of Extreme Precipitation Events in California and Relationships
844 with the Madden–Julian Oscillation. *J. Climate*, **13**, 3576–3587.

845 Kawai, Y. and A. Wada, 2007: Diurnal sea surface temperature variation and its impact on the
846 atmosphere and ocean: A review. *J. Oceanog.*, **63**, 721-744.

847 Khaiyer, M. M.,Minnis,R. Doelling, M. L. Nordeen, R. Palikonda,A. Rutan, and Y. Yi, 2010:
848 Improved TOA broadband shortwave and longwave fluxes derived from satellites over the
849 Tropical Western Pacific. *Proc. AMS 13th ConfRad.*, Portland, OR, June 27 – July 2, P1.16.

850 Khairoutdinov, M., and D. A. Randall, 2003: Cloud-resolving modeling of ARM Summer 1997
851 IOP: Model formulation, results, uncertainties and sensitivities. *J. Atmos. Sci.,* **60**, 607-625.

852 Klemp, J. B., J. Dudhia, A. D. Hassiotis, 2008, An upper gravity-wave absorbing layer for NWP
853 Applications, *Mon. Wea. Rev.*, *136*, 3987–4004.

854 Kim, D., A. H.Sobel, and I.-S.Kang (2011), A mechanism denial study on the Madden-Julian
855 Oscillation, *J. Adv. Model. Earth Syst.*, 3, M12007, doi:10.1029/2011MS000081.

856 Langley, R. B., R. W. King, I. I. Shapiro, R. D. Rosen, and D. A. Salstein (1981), Atmospheric
857 angular momentum and the length of the day: A common fluctuation with a period of 50 days,
858 *Nature,* **294**, 730 – 732

859 Lee, M.-I., I.-S. Kang, J.-K. Kim, and B. E. Mapes, 2001: Influence of cloud-radiation
860 interaction on simulating tropical intraseasonal oscillation with an atmospheric general
861 circulation model. *J. Geophys. Res.* , 106, D13, 14, 219-14, 233

862 Loeb, N. G., S. Kato, W. Su, T. Wong, F. G. Rose, D. R. Doelling, J. R. Norris, and X. Huang,
863 2012: Advances in understanding top-of-atmosphere radiation variability from satellite
864 observations. Surv. Geophys., 33, 359–385, doi:10.1007/ s10712-012-9175-1.

865 Lim, K-S S, S-Y Hong, 2010: Development of an Effective Double-Moment Cloud
866 Microphysics Scheme with Prognostic Cloud Condensation Nuclei (CCN) for Weather and
867 Climate Models. *Mon. Wea. Rev.*, **138**, 1587–1612.

868 Lin, H., and G. Brunet, 2009: The influence of the Madden–Julian oscillation on Canadian
869 wintertime surface air temperature. *Mon. Wea. Rev.,* **137**, 2250–2262

870 Lin, J-L and B. E. Mapes, 2004: Radiation Budget of the Tropical Intraseasonal Oscillation. *J.*
871 *Atmos. Sci.*, **61**, 2050–2062.

872 Lin, J-L and B. E. Mapes,, M. Zhang, and M. Newman, 2004: Stratiform Precipitation, Vertical
873 Heating Profiles, and the Madden–Julian Oscillation. *J. Atmos. Sci.*, **61**, 296–309.

874 Lin, J.-L., G.N. Kiladis, B.E. Mapes, K.M. Weickmann, K.R. Sperber, W. Lin, M.C. Wheeler,
875 S.D. Schubert, A. Del Genio, L.J. Donner, S. Emori, J.-F. Gueremy, F. Hourdin, P.J. Rasch, E.
876 Roeckner, and J.F. Scinocca, 2006: Tropical intraseasonal variability in 14 IPCC AR4 climate
877 models. Part I: Convective signals. *J. Climate*, **19**, 2665-2690, doi:10.1175/JCLI3735.1.

878 Ma, D. and Z. Kuang, Modulation of Radiative Heating by the Madden-Julian Oscillation and
879 Convectively Coupled Kelvin Waves as Observed by CloudSat, *Geophys. Res. Letts.*, 38,
880 L21813, (2011).

881 Madden, R. A., and P. R. Julian, 1971: Detection of a 40-50 day oscillation in the zonal wind in
882 the tropical Pacific. *J. Atmos. Sci.,* **28**, 702-708.

883 Madden, R. A., and P. R. Julian, 1972: Description of global-scale circulation cells in the tropics
884 with a 40-50 day period. *J. Atmos. Sci.,* **29**, 1109-1123.

885 Maloney, E. D., 2009: The moist static energy budget of a composite tropical intraseasonal
886 oscillation in a climate model. *J. Climate*, 22, 711–729.

887 Maloney, E. D., and D. L. Hartmann, 2000: Modulation of eastern North Pacific hurricanes by
888 the Madden–Julian oscillation. *J. Climate*, **13**, 1451–1460

889 Matsui, T., W.-K. Tao, and J. J. Shi: 2007: Goddard Radiation and Aerosol Direct Effect in
890 Goddard WRF, NASA/UMD WRF Meeting, Sep 14 2007.

891 Matthews, A., D. Baranowski, K. Heywood, P. Flatau, and S. Schmidtko, 2014: The surface
892 diurnal warm layer in the Indian Ocean during CINDY/DYNAMO. J. Climate.
893 doi:10.1175/JCLI-D-14-00222.1, in press.

894 Milbrandt, J. A., and M. K. Yau, 2005: A multimoment bulk microphysics parameterization. Part
895 I: Analysis of the role of the spectral shape parameter. *J. Atmos. Sci.*, **62,** 3051–3064.

896 Minnis, P., L. Nguyen, R. Palikonda, P. W. Heck, D. A. Spangenberg, D. R. Doelling,K. Ayers,
897 W. L. Smith, Jr., M. M. Khaiyer, Q. Z. Trepte, L. A. Avey, F.-L. Chang,R. Yost, T. L. Chee, and
898 S. Sun-Mack, 2008: Near-real time cloud retrievals from operational and research meteorological
899 satellites. *Proc. SPIE Europe Remote Sens. 2008*, Cardiff, Wales, UK, 15-18 September, **7107-2**,
900 8 pp.

901 Morrison, H., G. Thompson, and V. Tatarskii, 2009: Impact of cloud microphysics on the
902 development of trailing stratiform precipitation in a simulated squall line: Comparison of one-
903 and two-moment schemes. *Mon. Wea. Rev.*, 137, 991–1007.

904 Mrowiec, A. A., C. Rio, A. M. Fridlind, A. S. Ackerman, A. D. Del Genio, O. M. Pauluis, A. C.
905 Varble, and J. Fan (2012), Analysis of cloud-resolving simulations of a tropical mesoscale
906 convective system observed during TWP-ICE: Vertical fluxes and draft properties in convective
907 and stratiform regions, J. Geophys. Res., 117, D19201, doi:10.1029/2012JD017759.

908 Noh, Y., W. G. Cheon, S. Y. Hong, and S. Raasch, 2003, Improvement of the K profile model
909 for the planetary boundary layer based on large eddy simulation data, *Boundary Layer Meteorol.*,
910 107, 401–427.

911 Petch, J., Hill, A., Davies, L., Fridlind, A., Jakob, C., Lin, Y., Xie, S. and Zhu, P. (2014),
912 Evaluation of intercomparisons of four different types of model simulating TWP-ICE. *Q.J.R.*
913 *Meteorol. Soc.*, 140: 826–837. doi: 10.1002/qj.2192

914 Pohl, B., and A. J. Matthews, 2007: Observed changes in the lifetime and amplitude of the
915 Madden–Julian oscillation associated with interannual ENSO sea surface temperature anomalies,
916 *J. Climate*, **20**, 2659–2674

917 Powell, S. W., R. A. Houze, A. Kumar, and S. A. McFarlane (2012), Comparison of Simulated
918 and Observed Continental Tropical Anvil Clouds and Their Radiative Heating Profiles, *J. Atmos.*
919 *Sci.*, *69*(9), 2662-2681, doi:10.1175/jas-d-11-0251.1.

920 Powell, S. W., and R. A. Houze, Jr., 2013: The cloud population and onset of the Madden-Julian
921 Oscillation over the Indian Ocean during DYNAMO-AMIE. *J. Geophys. Res. Atmos.,* **118**,
922 11,979-11,995, doi:10.1002/2013JD020421.

923 Raymond, D. J., 2001: A new model of the Madden–Julian oscillation. *J. Atmos. Sci.,* **58,** 2807–
924 2819.

925 Rowe, A. K., and R. A. Houze, Jr., 2014: Microphysical characteristics of MJO convection over
926 the Indian Ocean during DYNAMO. *J. Geophys.Res. Atmos.,* **119**, 2543-2554,
927 doi:10.1002/2013JD020799.

928 Saunders, R. W., M. Matricardi, and P. Brunel, 1999: An improved fast radiative transfer model
929 for assimilation of satellite radiance observations. *Quart. J. Roy. Meteor. Soc.*,125, 1407–1426.

930 Schumacher, C., and R. A. Houze, Jr., 2003: Stratiform rain in the tropics as seen by the TRMM
931 Precipitation Radar. *J. Climate*, **16**, 1739-1756.

932 Shi, J. J., W.-K. Tao, T. Matsui, R. Cifelli, A. Hou, S. Lang, A. Tokey, N.-Y. Wang, C. Peters-
933 Lidard, G. Jackson, S. Rutledge, W. Petersen, 2010: WRF Simulations of the 20-22 January
934 2007 Snow Events over Eastern Canada: Comparison with in-s itu and Satellite Observations. J.
935 Applied Meteor. Climatol, 49, 2246-2266.

936 Skamarock, W. C., J. B. Klemp, J. Dudhia, D. O. Gill, D. M. Barker, M. G. Duda, X. Huang, W.
937 Wang, and J. G. Powers (2008), A description of the Advanced Research WRF version 3, *NCAR*
938 *Tech. Note NCAR/TN–475+STR*, 125 pp.

939 Smith, P. L., 1984: Equivalent radar reflectivity factors for snow and ice particles. *J. Climate*
940 *Appl. Meteor.*, 23, 1258–1260.

941 Sobel, A. H., S. Wang, and D. Kim, 2014: Moist static energy budget of the MJO during
942 DYNAMO. *J. Atmos. Sci.*, **71**, 4276-4291

943 Sobel, A. H., and H. Gildor 2003: A simple time-dependent model of SST hot spots. *Journal of*
944 *Climate*, **16**, 3978-3992.

945 Sobel, A. H., E. Maloney, G. Bellon and D.F.M. Frierson, 2008: The role of surface fluxes in
946 tropical intraseasonal oscillations. *Nature Geoscience*, **1**, 653-657.

947 Sobel, A.H., E. Maloney, G. Bellon and D.F.M. Frierson, 2010: Surface fluxes and tropical
948 intraseasonal variability: a reassessment. *Journal of Advances in Modeling Earth Systems*, **2**,
949 doi:10.3894/JAMES.2010.2.2.

950 Sobel, A. H. and E. Maloney, 2012: An idealized semi-empirical framework for modeling the
951 Madden-Julian oscillation. *J. Atmos. Sci.*, **69**, 1691-1705.

952 Sobel, A. H. and E. Maloney, 2013: Moisture modes and the eastward propagation of the MJO. *J.*
953 *Atmos. Sci.,* **70**, 187-192.

954 Sugiyama, M., 2009: Moisture mode in the tropics. Part I: Analysis based on the weak
955 temperature gradient approximation. J. Atmos. Sci., 66, 1507–1523.

956 Tao, W-K., D. Johnson, C-L. Shie, and J. Simpson (2004), The Atmospheric Energy Budget and
957 Large-Scale Precipitation Efficiency of Convective Systems during TOGA COARE, GATE,
958 SCSMEX, and ARM: Cloud-Resolving Model Simulations. *J. Atmos. Sci.*, *61*, 2405–2423.

959 Thompson, G., P. R. Field, R. M. Rasmussen, W. D. Hall. (2008) Explicit Forecasts of Winter
960 Precipitation Using an Improved Bulk Microphysics Scheme. Part II: Implementation of a New
961 Snow Parameterization. *Mon. Wea. Rev.*, **136**:12, 5095-5115.

962 Thorsen, T. J., Q. Fu, and J. Comstock (2011), Comparison of the CALIPSO satellite and
963 ground‐based observations of cirrus clouds at the ARM TWP sites, J. Geophys. Res., 116,
964 D21203, doi:10.1029/2011JD015970.

965 Van Diedenhoven, B., A.S. Ackerman, B. Cairns, and A.M. Fridlind, 2014: A flexible
966 parameterization for shortwave optical properties of ice crystals. J. Atmos. Sci., 71, no. 5, 1763-
967 1782, doi:10.1175/JAS-D-13-0205.1.Van Weverberg, K., A. M. Vogelmann, W. Lin, E. P. Luke,

968 A. Cialella, P. Minnis, M. Khaiyer, E. R. Boer, and M. P. Jensen, 2013: The role of cloud
969 microphysics parameterization in the simulation of mesoscale convective system clouds and
970 precipitation in the tropical western Pacific. *J. Atmos. Sci.*, **70,** 1104–1128

971 Varble, A., A. M. Fridlind, E. J. Zipser, A. S. Ackerman, J.-P. Chaboureau, J. Fan, A. Hill, S. A.
972 McFarlane, J.-P. Pinty, and B. Shipway (2011), Evaluation of cloud-resolving model
973 intercomparison simulations using TWP-ICE observations: Precipitation and cloud structure, *J.*
974 *Geophys. Res.*, 116, D12206, doi:10.1029/2010JD015180.

975 Varble, A., E.J. Zipser, A.M. Fridlind, P. Zhu, A.S. Ackerman, J.-P. Chaboureau, S. Collis, J.
976 Fan, A. Hill, and B. Shipway, 2014a: Evaluation of cloud-resolving and limited area model
977 intercomparison simulations using TWP-ICE observations. Part 1: Deep convective updraft
978 properties. *J. Geophys. Res. Atmos.*, **119**, no. 24, 13891-13918, doi:10.1002/2013JD021371.

979 Varble, A., E.J. Zipser, A.M. Fridlind, P. Zhu, A.S. Ackerman, J.-P. Chaboureau, J. Fan, A. Hill,
980 B. Shipway, and C. Williams, 2014b: Evaluation of cloud-resolving and limited area model
981 intercomparison simulations using TWP-ICE observations. Part 2: Precipitation microphysics. J.
982 Geophys. Res. Atmos., early on-line, doi:10.1002/2013JD021372.

983 Vitart, F., 2009: Impact of the Madden–Julian oscillation on tropical storms and risk of landfall
984 in the ECMWF forecast system. *Geophys. Res. Lett.,* **36**, L15802, doi:10.1029/2009GL039089.

985 Waldvogel, A., 1974: The N0 jump of raindrop spectra. J. Atmos. Sci., 31, 1067–1077.

986 Wang, S. and A. H. Sobel, 2011: Response of convection to relative SST: cloud resolving
987 simulations in 2D and 3D. *Journal of Geophysical Res*earch. 116, D11119.
988 DOI:10.1029/2010JD015347

989 Wang, S., and A. H. Sobel (2012), Impact of imposed drying on deep convection in a cloud-
990 resolving model, *Journal of Geophysical Res*earch, 117, D02112, doi:10.1029/2011JD016847.

991 Wang, S., A. H. Sobel, and Z. Kuang (2013), Cloud-resolving simulation of TOGA-COARE
992 using parameterized large-scale dynamics. *Journal of Geophysical Res*earch*,* 118,
993 doi:10.1002/jgrd.50510.

994 Wang, S., A. H. Sobel, F. Zhang, Y. Sun, Y. Yue, L. Zhou (2015). Regional simulation of the
995 October and November MJO events observed during the CINDY/DYNAMO field campaign at
996 gray zone resolution. *Journal of Climate*. **28**, 2097–2119.

997 Wang, Y., C. N. Long, L. R. Leung, J. Dudhia, S. A. McFarlane, J. H. Mather, S. J. Ghan, and X.
998 Liu, 2009: Evaluating regional cloud-permitting simulations of the WRF model for the Tropical
999 Warm Pool International Cloud Experiment (TWP-ICE), Darwin, 2006. J. Geophys. Res., 114,
1000 D21203doi:10.1029/2009JD012729.

1001 Wheeler, M. C., and J. L. McBride, 2005: Australian-Indonesian monsoon. Intraseasonal
1002 Variability in the Atmosphere-Ocean Climate System, W. K.-M. Lau and D. E. Waliser, Eds.,
1003 *Springer*, 125–173.

1004 Weickmann, Klaus, Edward Berry, 2009: The Tropical Madden–Julian Oscillation and the
1005 Global Wind Oscillation. *Mon. Wea. Rev.,* **137**, 1601–1614.

1006 Wielicki, B. A., B. R. Barkstrom, E. F. Harrison, R. B. Lee III, G. L. Smith, and J. E. Cooper,
1007 1996: Clouds and the Earth's Radiant Energy System (CERES): An earth observing system

1008 experiment. *Bull. Amer. Meteor. Soc.*, 77, 853–868, doi:10.1175/1520-
1009 0477(1996)077,0853:CATERE.2.0.CO;2.

1010 Wu, J., A. D. DelGenio, M.-S. Yao, and A. B. Wolf, 2009: WRF and GISS SCM simulations of
1011 convective updraft properties during TWP-ICE. *J. Geophys. Res.*, 114, D04206,
1012 doi:10.1029/2008JD010851.

1013 Wu, D., X. Dong, B. Xi, Z. Feng, A. Kennedy, G. Mullendore, M. Gilmore, and W.-K. Tao
1014 (2013), Impacts of microphysical scheme on convective and stratiform characteristics in two
1015 high precipitation squall line events, *J. Geophys. Res. Atmos.*, 118, 11,119–11,135,
1016 doi:10.1002/jgrd.50798.

1017 Wu, X., W. W. Grabowski, and M. W. Moncrieff (1998), Long-Term Behavior of Cloud
1018 Systems in TOGA COARE and Their Interactions with Radiative and Surface Processes. Part I:
1019 Two-Dimensional Modeling Study. *J. Atmos. Sci.*, *55*, 2693–2714.

1020 Xu, K-M, and D. A. Randall, 2001: Updraft and Downdraft Statistics of Simulated Tropical and
1021 Midlatitude Cumulus Convection. *J. Atmos. Sci.*, **58**, 1630–1649.

1022 Yoneyama, K., C. Zhang, and C. N. Long, 2013: Tracking pulses of the Madden-Julian
1023 oscillation. Bull. Amer. Meteor. Soc, 1871–1891, doi:10.1175/BAMS-D-12-00157.1

1024 Yoo, C., S. Feldstein, and S. Lee (2011), The impact of the Madden-Julian Oscillation trend on
1025 the Arctic amplification of surface air temperature during the 1979–2008 boreal winter, *Geophys.*
1026 *Res. Lett.,* **38**, L24804,

1027 Yuan, J and R. A. Houze Jr., 2013: Deep Convective Systems Observed by A-Train in the
1028 Tropical Indo-Pacific Region Affected by the MJO. *J. Atmos. Sci.*, **70**, 465–486.

1029 Yu, L., X. Jin, and R. A. Weller, 2008: Multidecade Global Flux Datasets from the Objectively
1030 Analyzed Air-sea Fluxes (OAFlux) Project: Latent and sensible heat fluxes, ocean evaporation,
1031 and related surface meteorological variables. Tech. rep., Woods Hole Oceano graphic Institution,
1032 OAFlux Project Technical Report. OA-2008-01, 64pp. Woods Hole. Massachusetts.

1033 Zeng, X., W-K Tao, M. Zhang, A. Y. Hou, S. Xie, S. Lang, X. Li, D. O'C. Starr, X. Li, and J.
1034 Simpson, 2009: An Indirect Effect of Ice Nuclei on Atmospheric Radiation. *J. Atmos. Sci.*, **66**,
1035 41–61.

1036 Zhang, C., 2005: Madden–Julian oscillation. *Rev. Geophys*., **43**, RG2003,
1037 doi:10.1029/2004RG000158.

1038 Zhang, C. and M. Dong, 2004: Seasonality in the Madden–Julian oscillation. *J. Climate*, **17**,
1039 3169–3180

1040 Zhang, C., J. Gottschalck, E. D. Maloney, M. W. Moncrieff, F. Vitart, D. E. Waliser, B. Wang,
1041 and M. C. Wheeler, 2013: Cracking the MJO nut. Geophys. Res. Lett., 40, 1223–1230,
1042 doi:DOI:10.1002/grl.50244.

1043 Zhao, C., et al. (2012), Toward understanding of differences in current cloud retrievals of ARM
1044 ground-based measurements, *J. Geophys. Res.,* 117, D10206, doi:10.1029/2011JD016792.

1045 Zhu, P., J. Dudhia, P. Field, K. Wapler, A. Fridlind, A. Varble, E. Zipser, J. Petch, M. Chen, and
1046 Z. Zhu, 2012: A limited area model (LAM) intercomparison study of a TWP-ICE active

1047 monsoon mesoscale convective event. *J. Geophys. Res.*, **117**, no. D11, D11208,
1048 doi:10.1029/2011JD016447.

1049 Zuluaga, M. D., and R. A. Houze, Jr., 2013: Evolution of the population of precipitating
1050 convective systems over the Equatorial Indian Ocean in Active Phases of the Madden-Julian
1051 Oscillation. *J. Atmos Sci.*, **70**, 2713–2725.

1052

Table 1 Number concentration of the hydrometeor species in the microphysics schemes adopted in this study (Nc, cloud water; Nr, rainwater; Ni, cloud ice; Ng, graupel; Ns, snow; Nh, hail). Most of these schemes have same number of hydrometeors, except that hail is also simulated by MY05. WDM6 has 2M treatment of cloud water and rain, but 1M treatment of all ice species.

	Cloud droplet (cm^{-3})	Diagnosed number concentration of hydrometeors	Predicted number concentration of hydrometeors
PLin	100	Nc, Nr, Ni, Ng, Ns	−
WSM6	−	Nc, Nr, Ni, Ng, Ns	−
WDM6	−	Ni, Ng, Ns	Nc, Nr
Morrison	250	Nc	Nr, Ni, Ng, Ns
MY05	200	−	Nc, Nr, Ni, Ng, Ns, Nh
Thompson	100	Nc, Ng, Ns	Nr, Ni

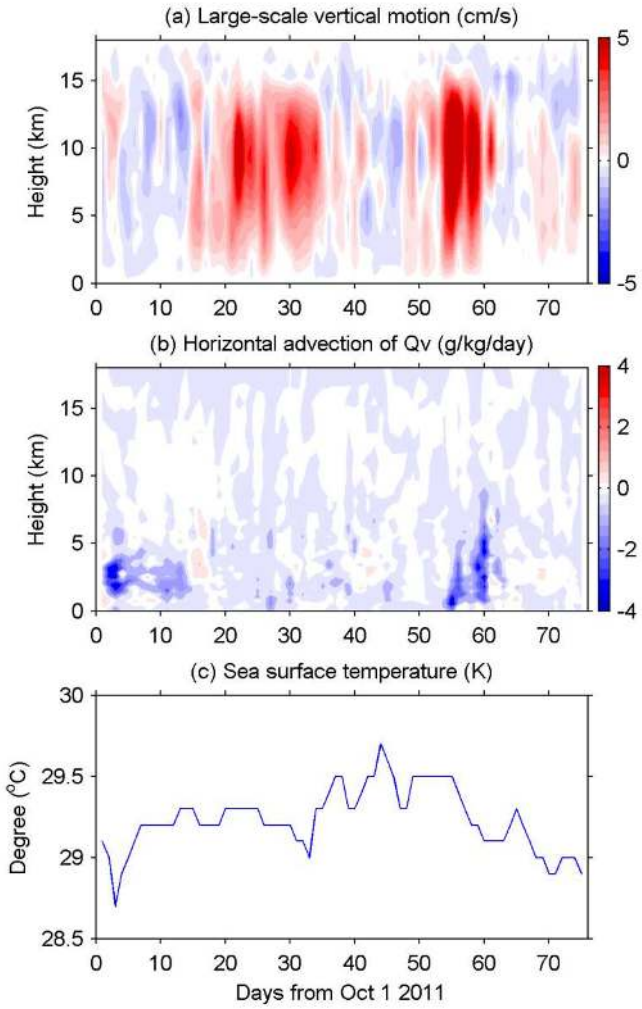

Figure 1. (a) Large-scale vertical motion (cm/s) from northern sounding array. (b) Horizontal advection of moisture (g/kg/day). (c) Daily sea surface temperature (°C).

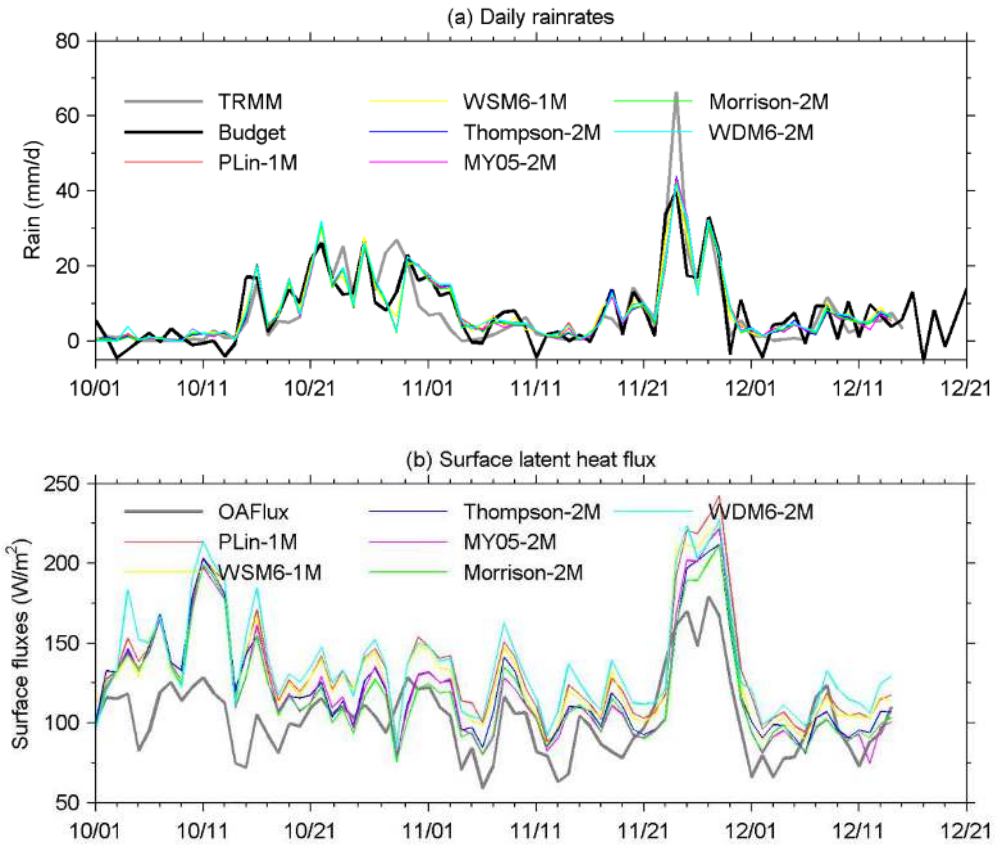

Figure 2. Time series of domain averaged (a) surface rain rates and (b) turbulent fluxes. The TRMM 3B43V7 data is shown in gray, and budget derived rain rate in black. Total surface fluxes from the OAFlux data is shown in gray in (b).

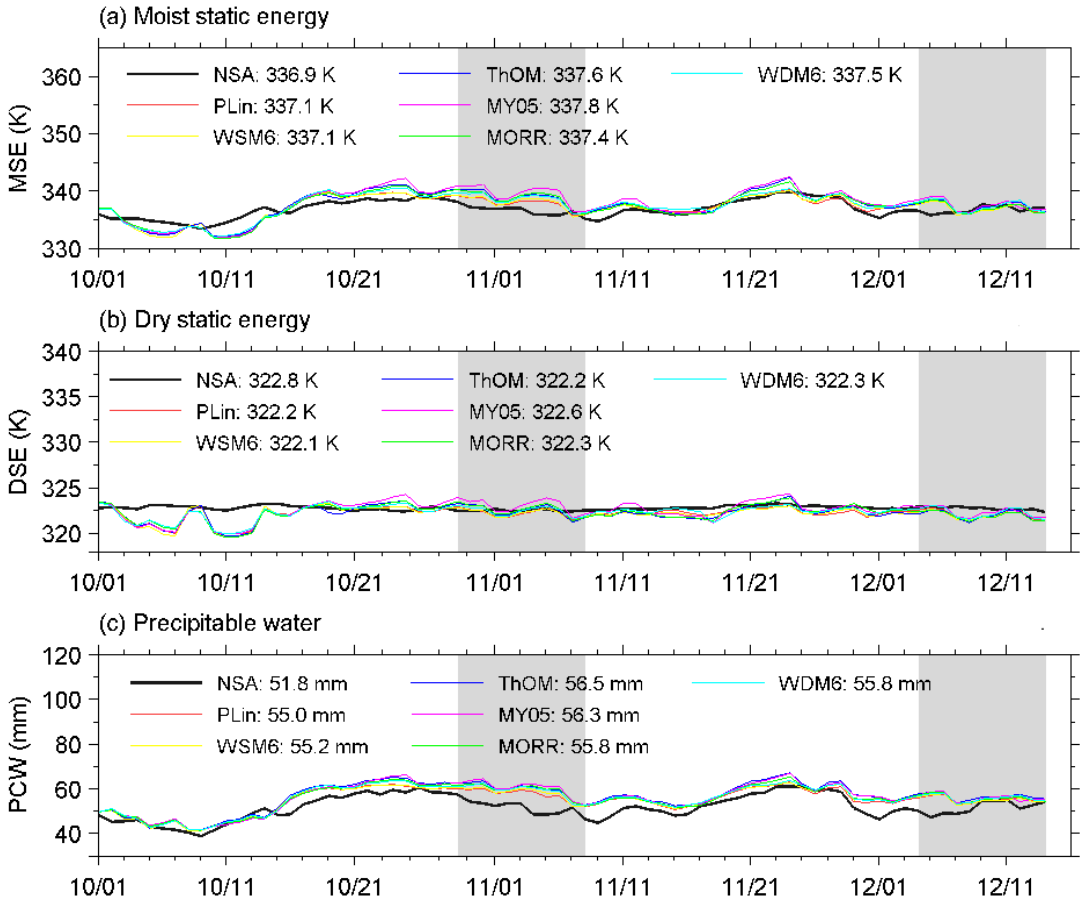

Figure 3. Biases in column-integrated moist static energy (K), dry static energy (K), total precipitation water (mm). Shaded area indicates periods when R/V Reville is off station and the forcing uncertainty is expected to be larger than the rest period.

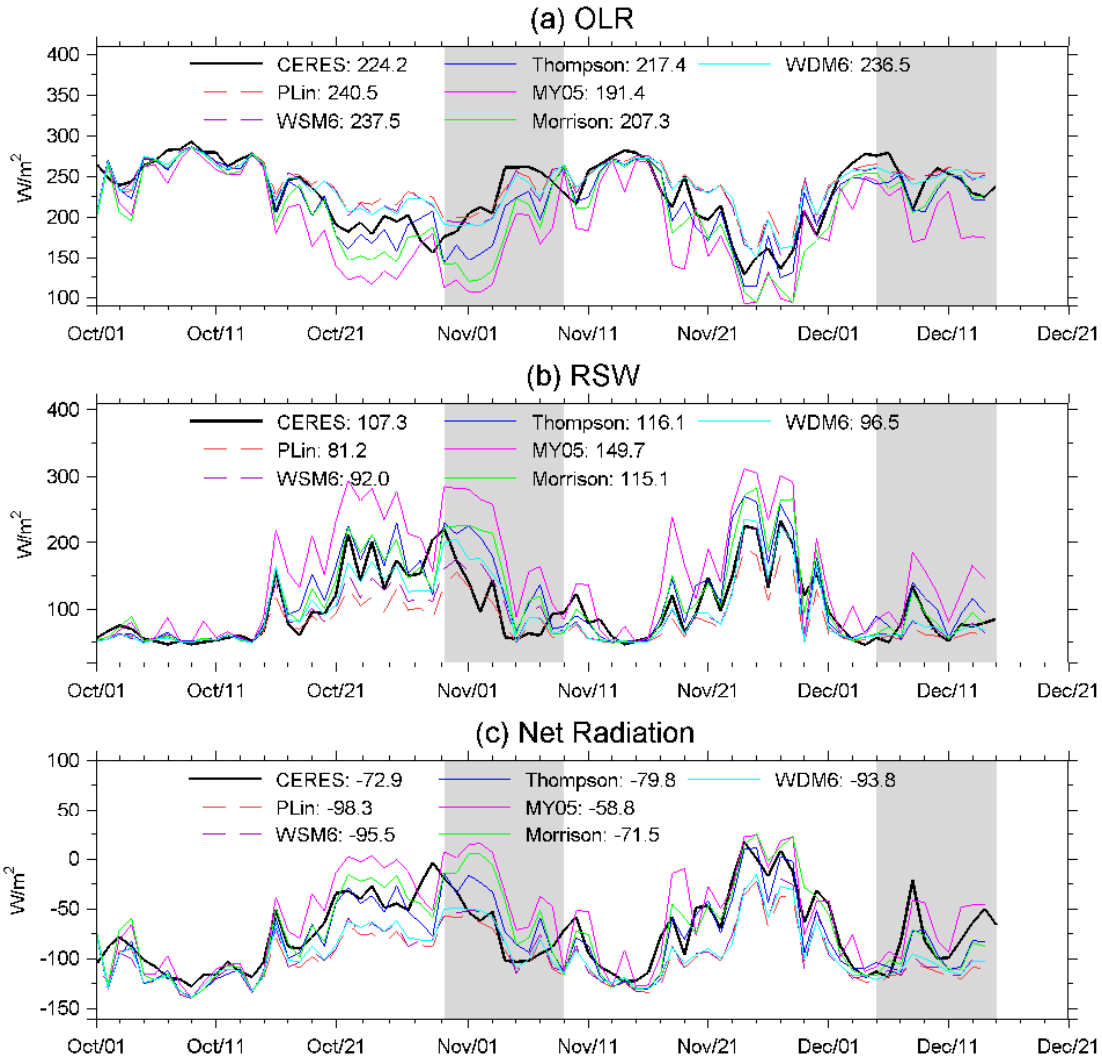

1070

1071 **Figure 4.** Time series of daily (a) OLR, (b) RSW, and (c) column net radiation from all the model
1072 experiments. Shaded areas indicates period when R/V Revelle was off station.

1073

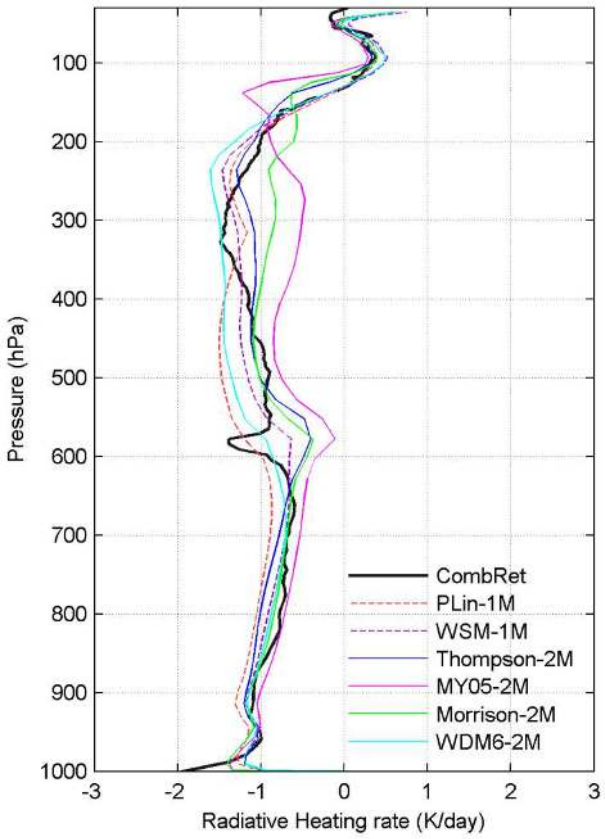

1074

1075 **Figure 5.** Vertical profiles of time mean radiative heating profiles from the simulations and the
1076 Combined Retrieval.

1077

1078

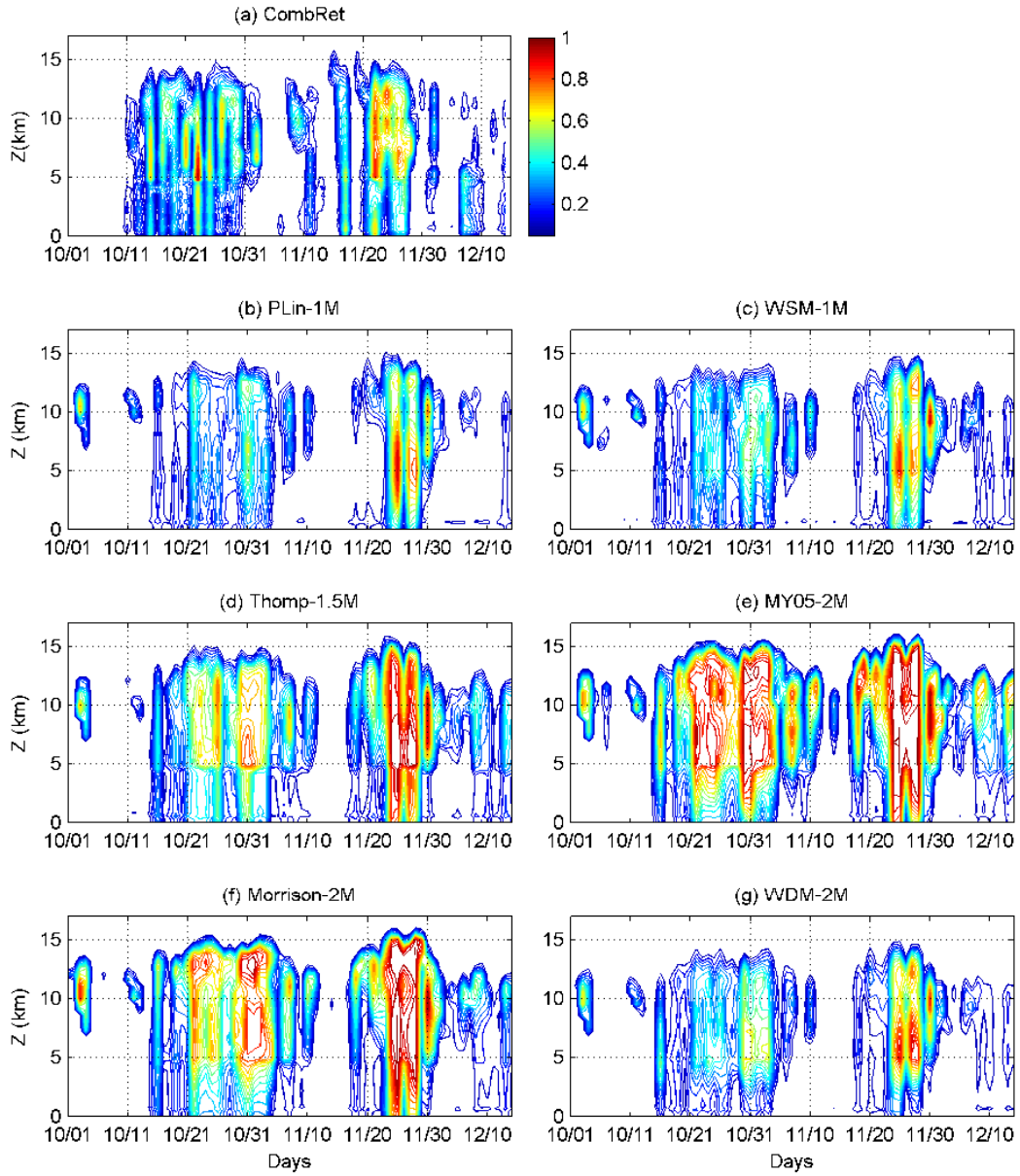

Figure 6. (a) Daily mean cloud fraction from CombRet, as the ration between number of cloudy points (defined as IWC and LWC greater than 0.005 g/kg) and the number (2880) of observations over a day. (b-g): Time series of cloud fraction (defined using the threshold rain+snow+graupel+cloud wate+cloud ice > 0.005 g/kg) for all the numerical experiments, defined as cloudy points divided by total grid points.

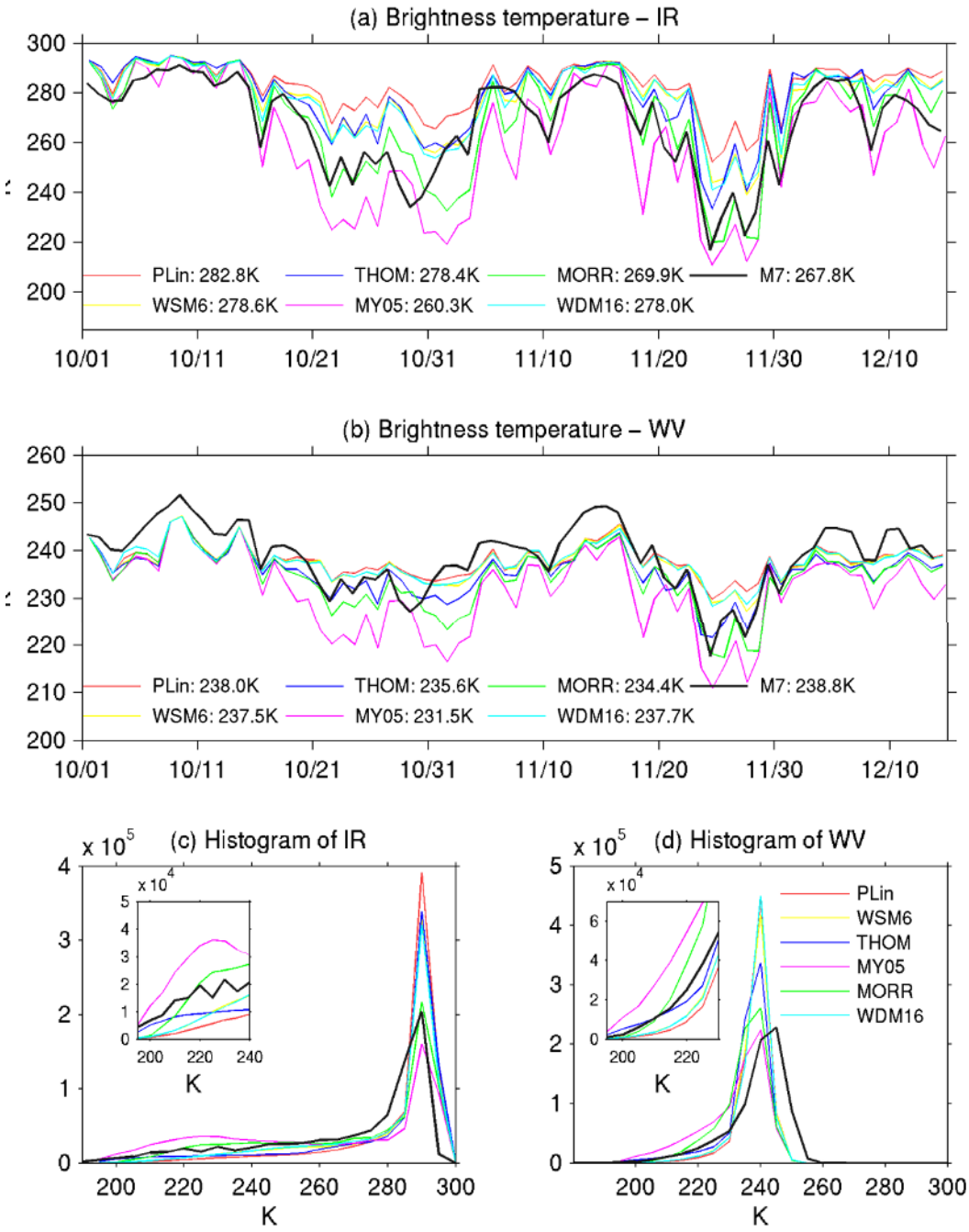

Figure 7. Time series of daily mean brightness temperature (Tb) from the MVIRI (a) IR and (b) WV bands. Probability distributions of MVIRI (c) IR and (d) WV Tb values. Black curve indicates Tb from Meteosat-7 averaged over the NSA domain. Inserts show zoom-in views of the histogram at the lower end of the Tb histogram.

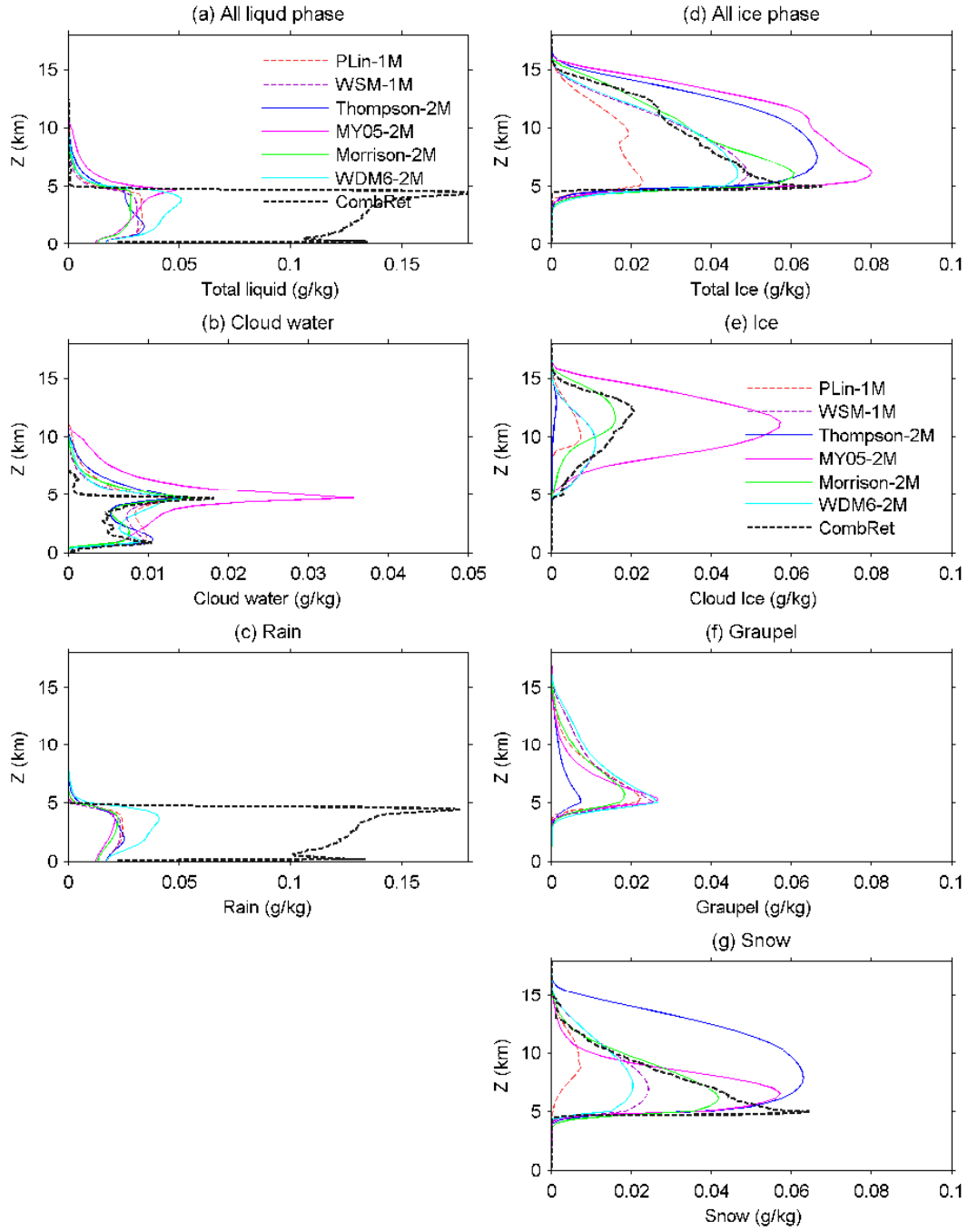

1091

1092 **Figure 8.** Time and domain averaged liquid phase hydrometeor concentrations (left column) and
1093 all ice phase hydrometeors (right column) for all the numerical experiments. Cloud ice from
1094 WSM6 and WDM6 overlay each other as their difference is small. Hail is grouped with graupel
1095 in MY05.

1096

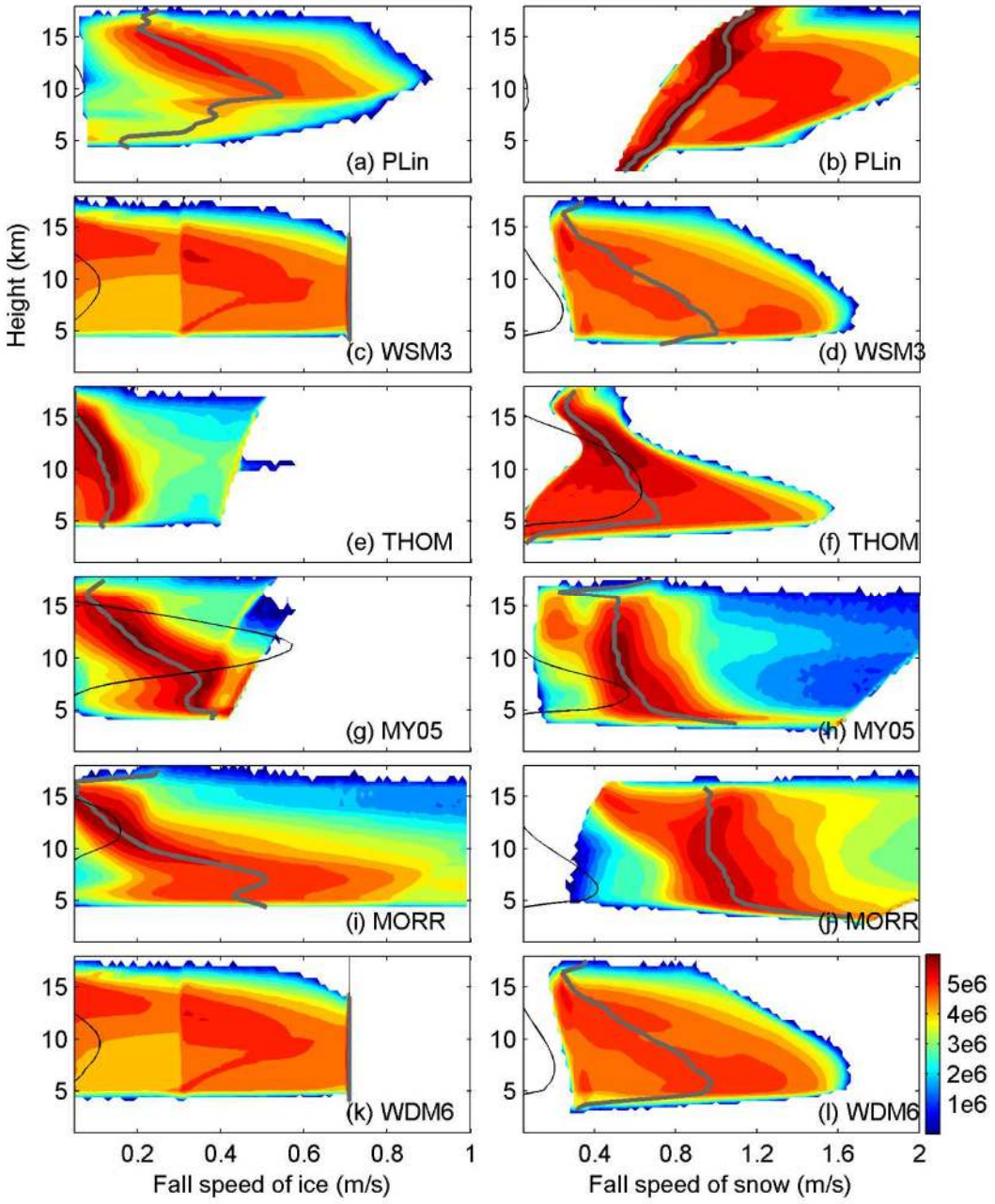

Figure 9. Histogram of terminal fall speeds of (left column) cloud ice and (right column) snow for all simulations. Grey curves indicate median values of the fall speeds. The black curves are ice and snow mixing ratio times 10^4(kg/kg). The color scale is logarithmic.

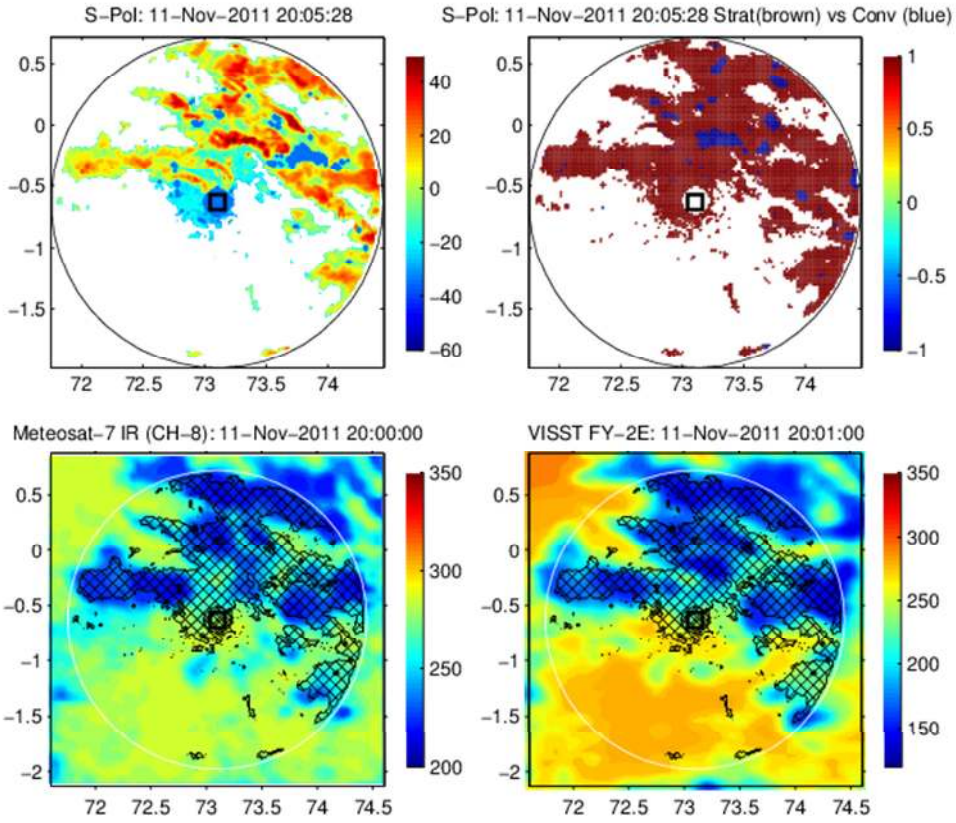

Figure 10. (a) S-Polka radar reflectivity at 2.5 km. (b) Stratiform and convective echoes. (c) Inferred radiation at Channel-8 from Meteosat-7. The hatched area in the bottom 2 panels corresponds to cloudy points identified as either stratiform or convective echoes in (b). (d) as (c), but for FY-2E broadband TOA OLR.

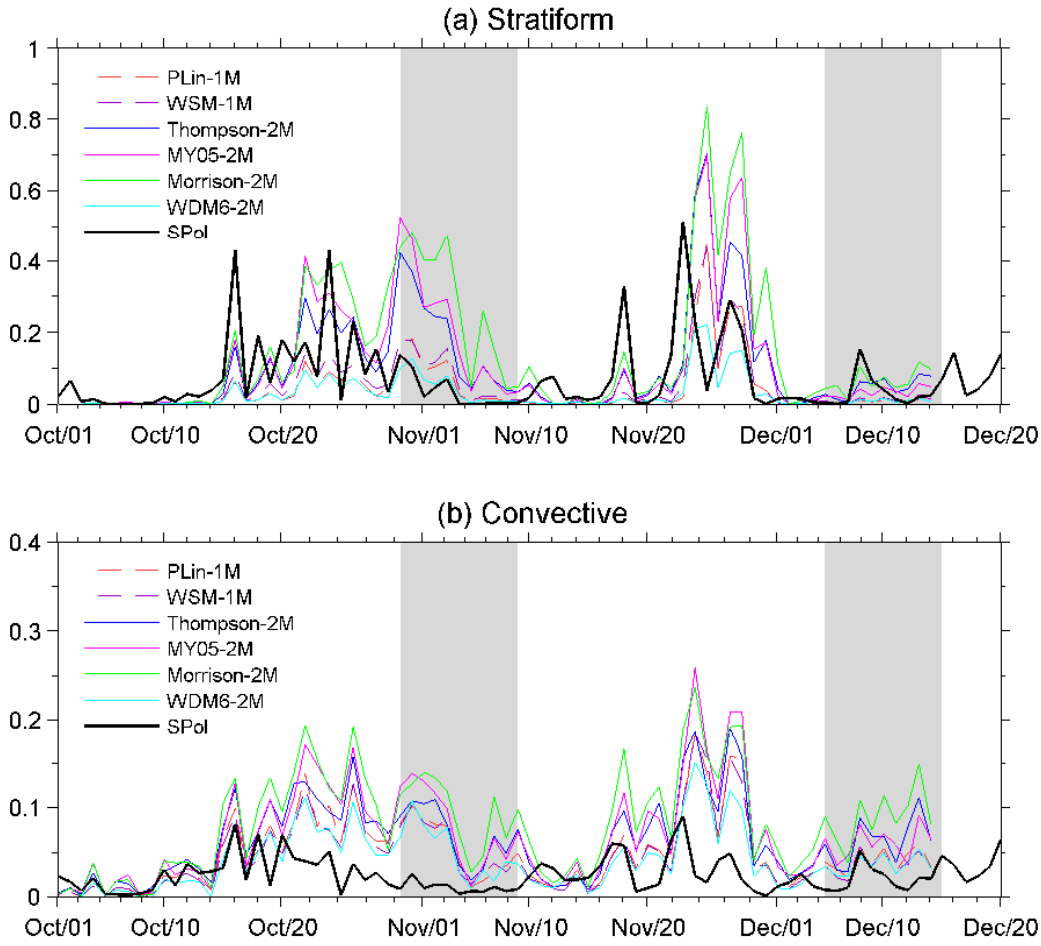

Figure 11. Area fraction of (a) stratiform and (b) convective echoes from the model simulations with various microphysics schemes. The stratiform and convective echoes from S-Polka (black) are also shown for reference. Because S-Polka is located at Gan, the southwest corner of the NSA, model simulations and radar data are not expected to match.

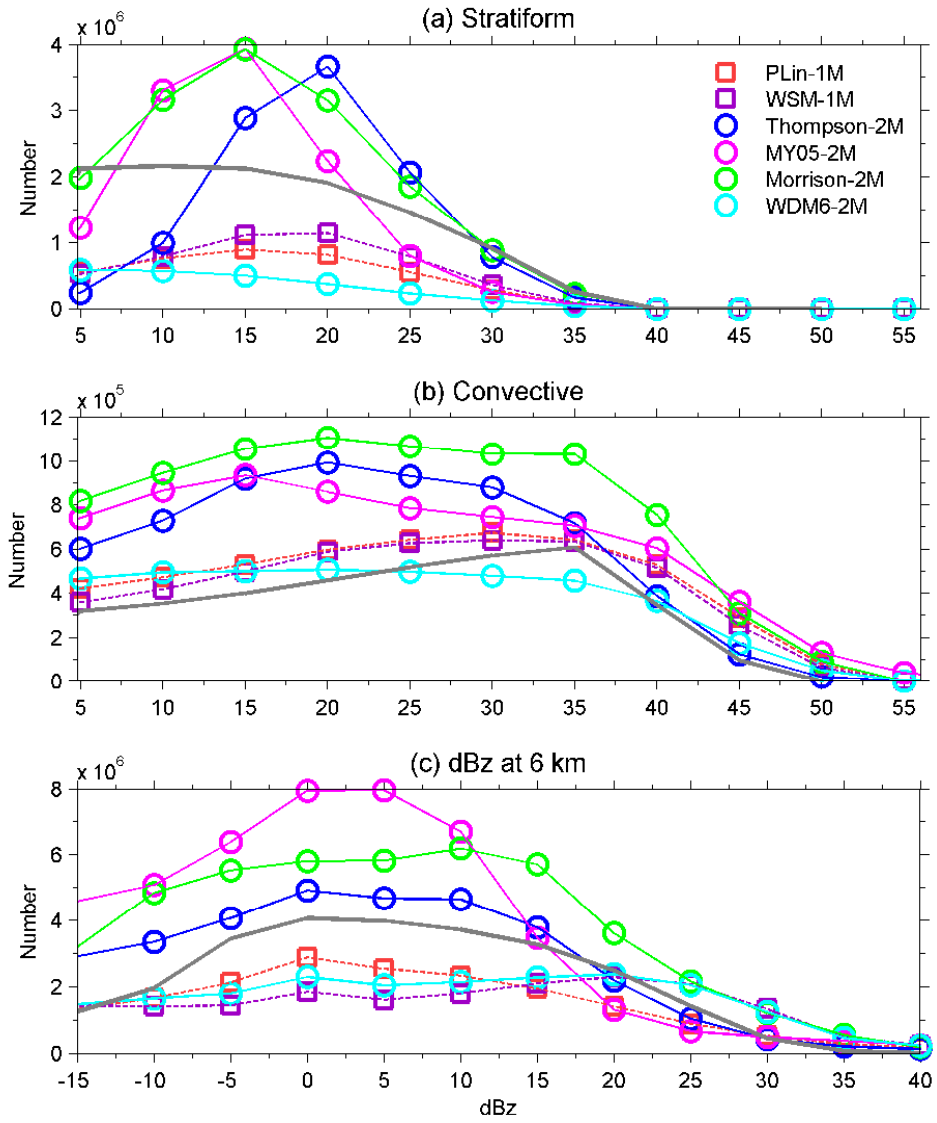

1114

1115 **Figure 12**. Histogram of (a) stratiform and (b) convective dBz events from model and S-Polka
1116 radar identified using the texture based CS algorithm (gray) with additional requirement that dBz
1117 should exceed 5 dBz at 6 km. (c) Histogram of dBz events at 6 km from model and S-Polka.
1118 Model-simulated radar echo number has been rescaled according to time and spatial sampling as
1119 well as rain rates.

1120

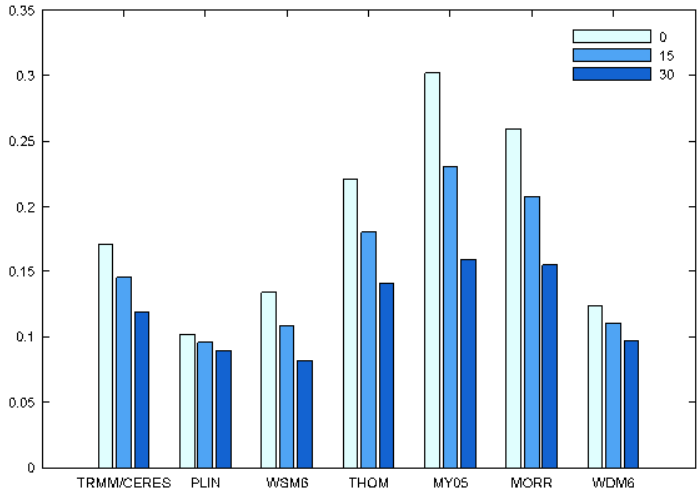

1121

1122 **Figure 13**. Radiative feedback derived from CERES/TRMM and 6 model simulations as the
1123 linear coefficient of column net radiation and precipitation (both in W/m^2) using a least-square
1124 2^{nd} order polynomial fit for rain rates at 0, 15, and 30 mm/day.

1125

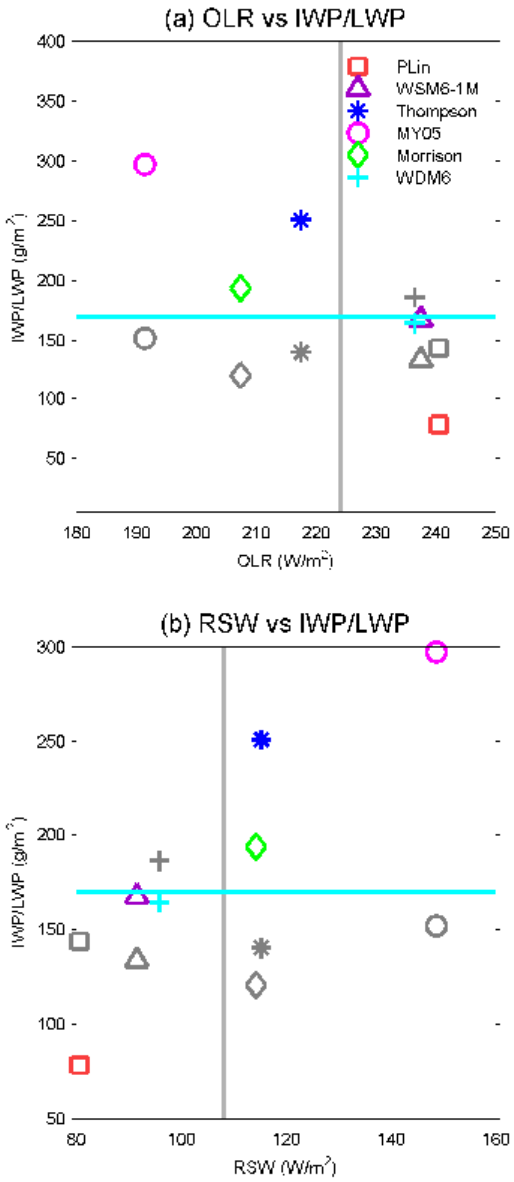

Figure 14. Top: OLR vs IWP (Ice water path) and LWP (liquid water path). Bottom: as top, but for RSW. Color symbols indicate IWP, and gray symbols, LWP. The grey vertical lines indicate the time mean values from CERES SYN1deg. Cyan line indicates IWP from CombRet. LWP from CombRet is too large, (~572 g/m2) thus not shown in the figure.

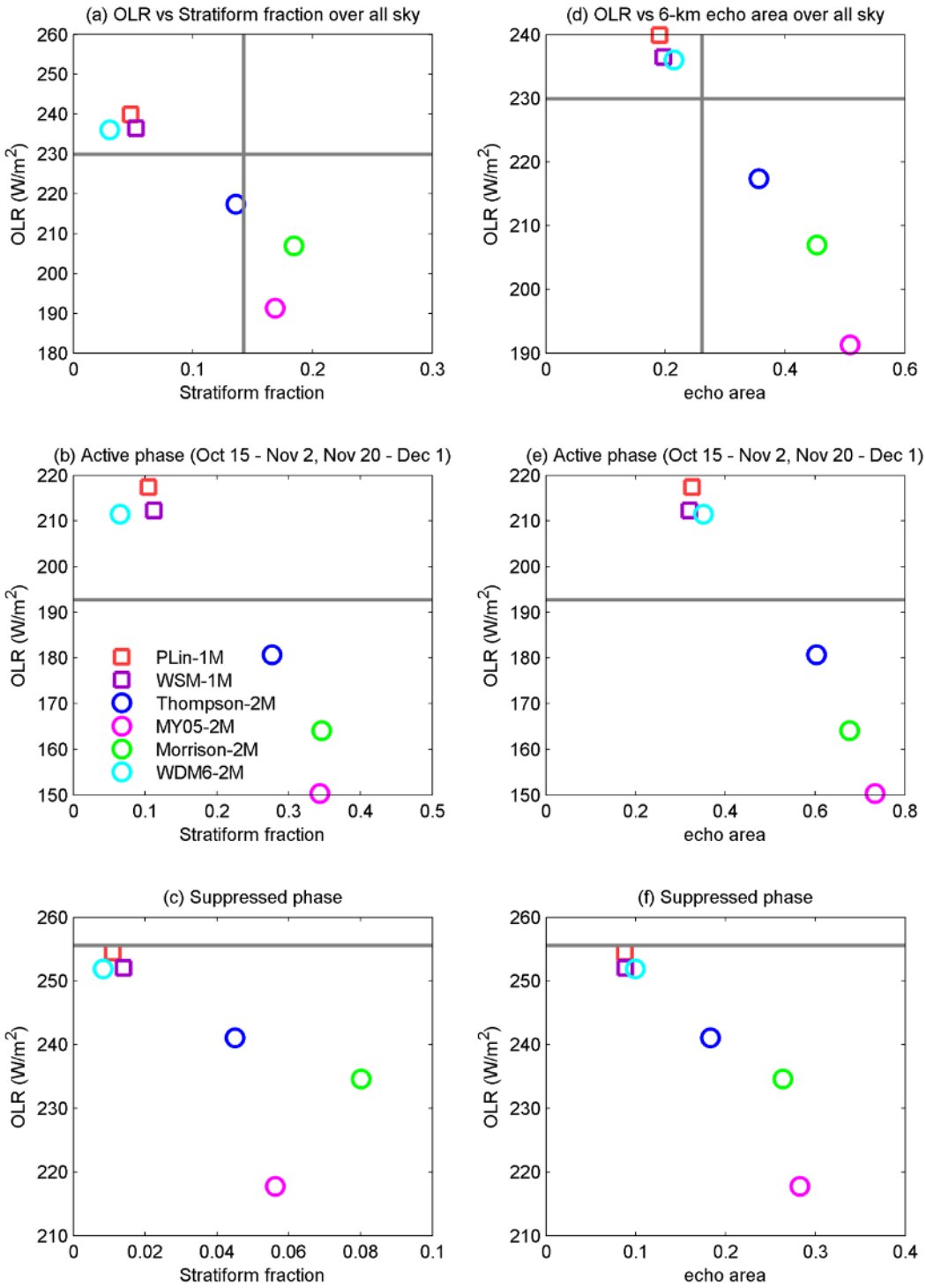

1133

1134 **Figure 15**. Left column: stratiform area fraction vs domain averaged OLR for (a) the entire period, (b)
1135 active phase (Oct 15 – Nov 2, Nov 20 – Dec 1), and (c) suppressed phase. Right column, as the left
1136 column, but for 6 –km radar echoes vs domain averaged OLR.

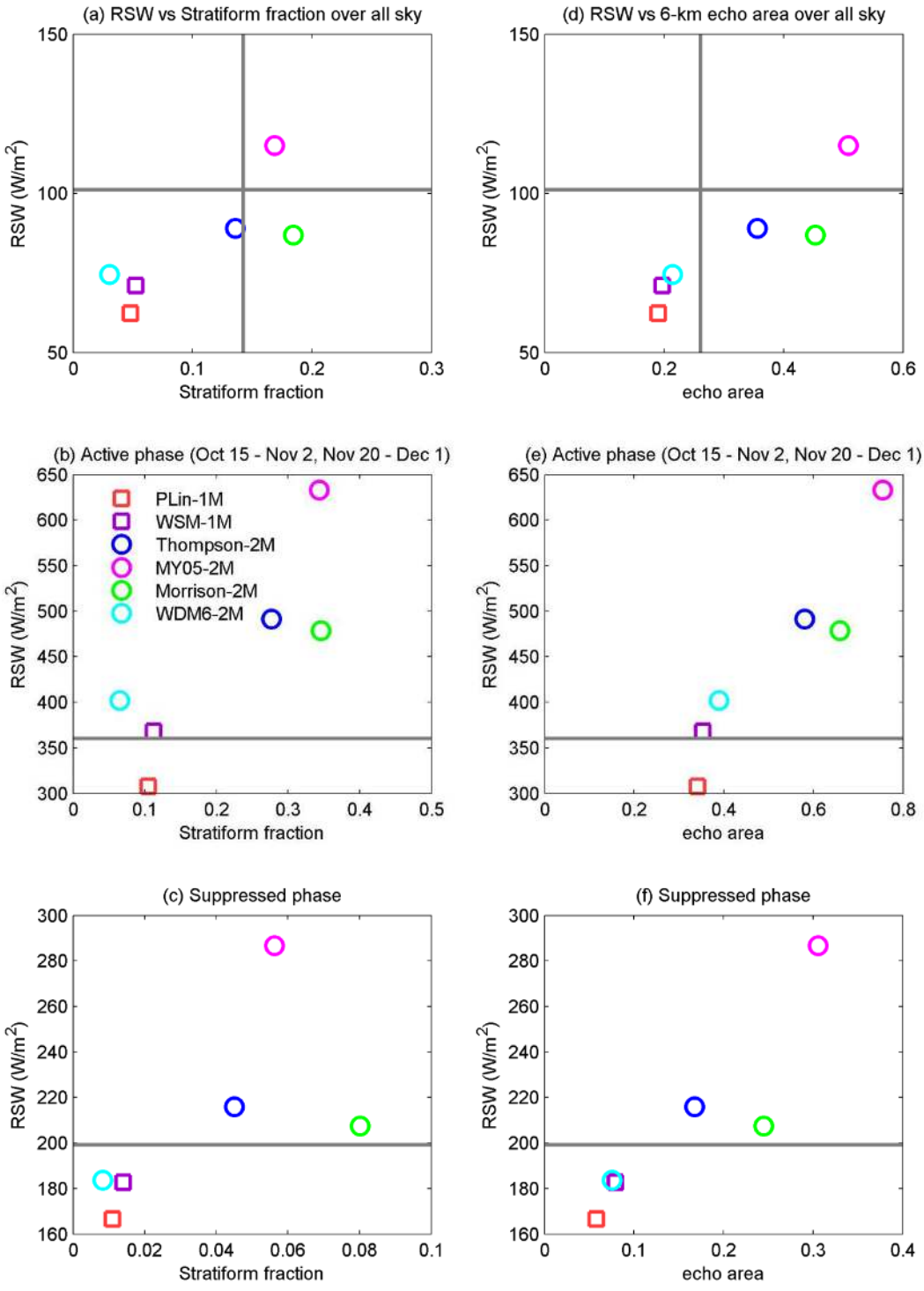

Figure 16. Left column: stratiform area fraction vs domain averaged RSW at local time 11 am for (a) the entire period, (b) active phase (Oct 15 – Nov 2, Nov 20 – Dec 1), and (c) suppressed phase. Right column, as the left column, but for 6 km radar echoes vs domain averaged OLR.

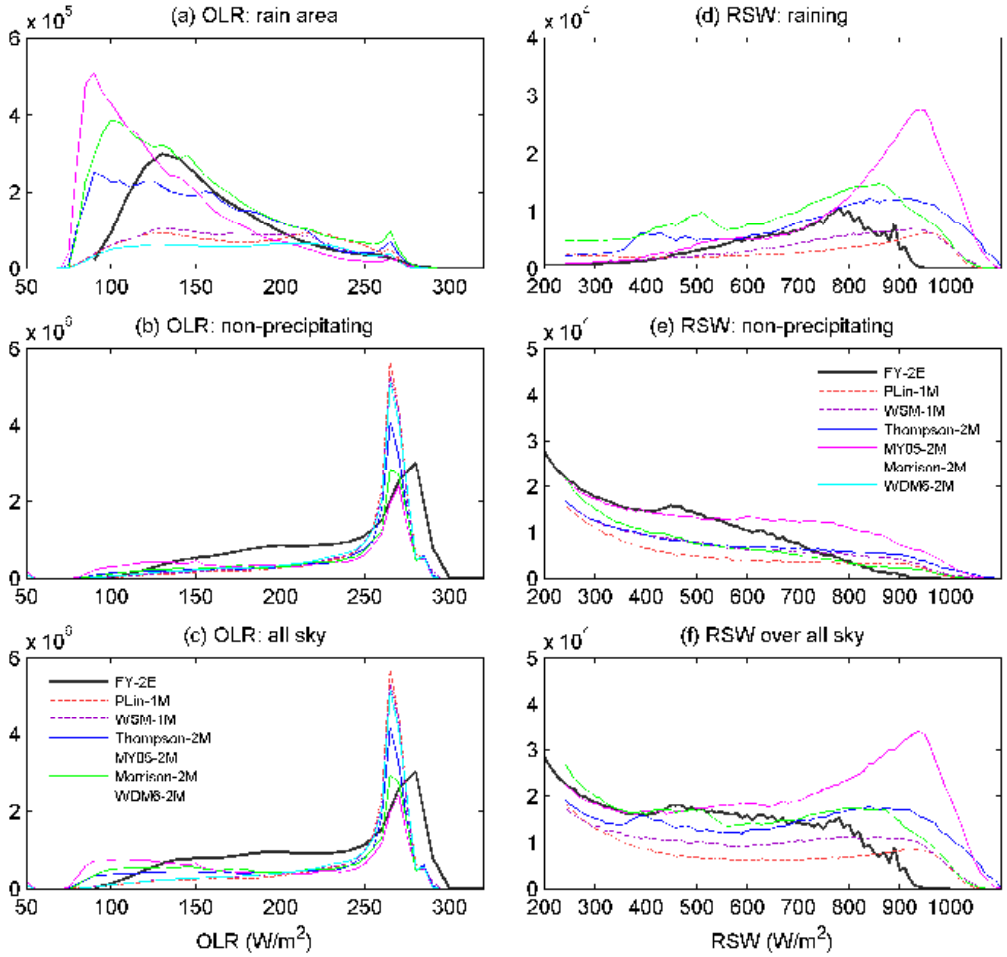

1141

1142 **Figure 17**. Left column: histogram of OLR over (a) rainy region, (b) non-precipitating region,
1143 and (c) all sky. Black: OLR from FY-2E conditioned by the S-Polka radar echoes. Right column:
1144 histogram of TOA reflected short wave (RSW) at local time 11 LST over (a) cloudy regions, (b)
1145 non-precipitating regions, and (c) all sky. Black: RSW from VISST conditioned by the S-Polka
1146 radar echoes.